Extra-Nuclear Starbursts: Young Luminous Hinge Clumps in Interacting Galaxies

Beverly J. Smith[1], Roberto Soria[2], Curtis Struck[3], Mark L. Giroux[1], Douglas A. Swartz[4], and Mihoko Yukita[5]

ABSTRACT

Hinge clumps are luminous knots of star formation near the base of tidal features in some interacting galaxies. We use archival Hubble Space Telescope UV/optical/IR images and Chandra X-ray maps along with GALEX UV, Spitzer IR, and ground-based optical/near-IR images to investigate the star forming properties in a sample of 12 hinge clumps in five interacting galaxies. The most extreme of these hinge clumps have star formation rates of $1 - 9$ $M_\odot$ yr^{-1}, comparable to or larger than the 'overlap' region of intense star formation between the two disks of the colliding galaxy system the Antennae. In the HST images, we have found remarkably large and luminous sources at the centers of these hinge clumps. These objects are much larger and more luminous than typical 'super-star clusters' in interacting galaxies, and are sometimes embedded in a linear ridge of fainter star clusters, consistent with star formation along a narrow caustic. These central sources have diameters of ∼70 pc, compared to ∼3 pc in 'ordinary' super-star clusters. Their absolute I magnitudes range from $M_I \sim -12.2$ to -16.5, thus if they are individual star clusters they would lie near the top of the 'super star cluster' luminosity function of star clusters. These sources may not be individual star clusters, but instead may be tightly packed groups of clusters that are blended together in the HST images. Comparison to population synthesis modeling indicates that the hinge clumps contain a range of stellar ages. This is consistent with expectations based on models of galaxy interactions, which suggest that star formation may be prolonged in these regions. In the Chandra images, we have found strong X-ray emission from several of these hinge clumps. In most cases, this emission is well-resolved with Chandra and has a thermal X-ray spectrum, thus it is likely due to hot gas associated with the star formation. The ratio of the extinction-corrected diffuse X-ray luminosity to the mechanical energy rate (the X-ray production efficiency) for the hinge clumps is similar to that in the Antennae galaxies, but higher than those for regions in the normal spiral galaxy NGC 2403. Two of the hinge clumps have point-like X-ray emission much brighter than expected for hot gas; these sources are likely 'ultra-luminous X-ray sources' (ULXs) due to accretion disks around black holes. The most extreme of these sources, in Arp 240, has a hard X-ray spectrum and an absorbed X-ray luminosity of $\sim 2 \times 10^{41}$ erg s^{-1}; this is above the luminosity expected by single high mass X-ray binaries (HMXBs), thus it may be either a collection of HMXBs or an intermediate-mass black hole ($\geq$80 $M_\odot$).

Subject headings: galaxies: individual (Arp 82, Arp 240, Arp 244, Arp 256, Arp 270, NGC 2207, NGC 2403)–galaxies: interactions–galaxies: starburst

[1]Department of Physics and Astronomy, East Tennessee State University, Johnson City TN 37614; smithbj@etsu.edu; girouxm@etsu.edu

[2]Curtin Institute of Radio Astronomy, Curtin University, 1 Turner Avenue, Bentley, WA 6102, Australia; rosoria@physics.usyd.edu.au

[3]Department of Physics and Astronomy, Iowa State University, Ames IA 50011; curt@iastate.edu

[4]University Space Research Association, NASA Marshall Space Flight Center, ZP 12, Huntsville AL

[5]Department of Physics and Astronomy, Johns Hopkins

1. Introduction

Some of the most luminous extra-nuclear star forming regions known in the local Universe lie near the base of tidal structures in interacting galaxies. We have dubbed these regions 'hinge clumps' as they lie near the 'hinge' of the tail (Hancock et al. 2009; Smith et al. 2010). Hinge clumps can have $L_{H\alpha} > 10^{40}$ erg/s (Hancock et al. 2007), earning them the label of extra-nuclear starbursts. Their location on the outskirts of galaxy disks means they may be important in enriching the intergalactic medium via winds. Hinge clumps may be more extreme sites of star formation than 'tidal dwarf galaxies', larger but lower density star forming regions found near the ends of tidal features. Hinge clumps may be as common as tidal dwarfs, but are not nearly as well-studied. Hinge clumps bear an intriguing resemblance to the massive star forming regions formed by gravitational instabilities in high redshift disks (e.g., Cowie et al. 1995; Elmegreen et al. 2009; Föster Schreiber et al. 2011; Elmegreen & Elmegreen 2014), thus the study of these regions broadens our perspective on high redshift disk evolution.

Our recent analytical models of galaxy interactions (Struck & Smith 2012) have provided insights into why star formation is so intense in these regions. These models sometimes produce intersecting caustics near the base of tidal tails, where a caustic is a narrow pile-up zone produced by orbit crowding. Intersecting gas flows within or between caustics may trigger star formation at these locations, producing hinge clumps. In retrospect, evidence for overlapping waves or compressions in the hinge regions of tidal tails can also be seen in many classical papers that modeled galaxy flybys (e.g., Toomre & Toomre 1972; Elmegreen et al. 1991; Gerber & Lamb 1994). More generally, the higher velocity dispersions in the interstellar gas in interacting galaxies may lead to more massive self-gravitating clouds (Elmegreen, Kaufman, & Thomasson 1993; Bournaud, Duc, & Emsellem 2008; Teyssier, Chapon, & Bournaud 2010), and therefore more efficient star formation and more luminous star forming regions in interacting systems compared to more isolated galaxies.

Numerical and analytical models show that intersecting caustics can be produced in both the inner regions of interacting galaxies as well as in tidal features. Strong prograde encounters can produce 'ocular' structures in disks: eye-shaped ovals formed from intersecting spiral arms (Elmegreen et al. 1991). Luminous knots of star formation are sometimes observed along the 'eyelids' and in the 'points' of oculars (Elmegreen et al. 2006; Hancock et al. 2007, 2009). In tidal features, models reveal a wide variety of caustic morphologies. A single strong caustic is sometimes produced along the leading edge of tidal features; in other cases, two approximately parallel caustics or two diverging or branching caustics are seen in tidal tails (Elmegreen et al. 1991; Donner, Engstrom, & Sundelius 1991; Gerber & Lamb 1994; Struck & Smith 2012). In some tidal features, a diverging caustic branches back towards the main disk, creating a loop-like structure, while in other cases two caustics diverge to produce a double-tail morphology (Struck & Smith 2012). Models also sometimes show a 'narrowing' of a tidal feature where two caustics converge (Gerber & Lamb 1994; Struck & Smith 2012). At such intersections between caustics, gas build-up and gravitational collapse is expected to occur, triggering star formation. Converging caustics can also occur in the outer portions of tidal features, potentially producing knots of star formation (Struck & Smith 2012), but most tidal dwarfs may form via gas accumulation and gravitational collapse near the end of a tidal feature (Duc, Bournaud, & Masset 2004; Bournaud & Duc 2006; Wetzstein, Naab, & Burket 2007).

Continued gas inflow into hinge clumps along caustics may produce sustained star formation in these regions, rather than instantaneous bursts. High spatial resolution imaging is one way to test this hypothesis. At high spatial resolution, knots of star formation in nearby galaxies resolve into multiple young star clusters (Zhang et al. 2001; Larsen 2004; Bastian et al. 2005; Mullan et al. 2011). The most luminous of these young clusters are termed 'super star clusters' or 'young massive clusters' (e.g., Larsen 2000). For clumps of star formation in the disk of Arp 284W, the average age of the stars in the clump derived from single-burst stellar population synthesis models is older than that found for the observed star

University, Baltimore MD 21218; myukita1@pha.jhu.edu

clusters in that clump seen in Hubble Telescope images (Peterson et al. 2009). This indicates that more than one generation of stars is present in the region, with the older clusters fading and possibly dissolving with time but still contributing to the total light of the clump.

Regions with sustained star formation may have strong X-ray emission, as very young stars may exist simultaneously with the end products of stellar evolution. Given the high star formation rates in hinge clumps, strong diffuse x-ray emission may be present due to stellar winds, supernovae, and shocks. In spiral and irregular galaxies, the diffuse X-ray luminosity correlates with the star formation rate (Strickland et al. 2004; Owen & Warwick 2009; Mineo, Gilfanov, & Sunyaev 2012b).

Hinge clumps may also host bright X-ray point sources, as the number of high mass X-ray binaries (HMXBs) is correlated with the star formation rate in spiral galaxies (Grimm, Gilfanov, & Sunyaev 2003; Gilfanov, Grimm, & Sunyaev 2004; Persic et al. 2004; Mineo, Gilfanov, & Sunyaev 2012a). The number of 'ultra-luminous' X-ray point sources (ULXs; $L_X \geq 10^{39}$ erg s^{-1}) is also correlated with the star formation rate in both normal spirals and pre-merger interacting galaxies (Swartz et al. 2004, 2011; Liu, Bregman, & Irwin 2006; Smith et al. 2012). This correlation suggests that most ULXs are X-ray luminous HMXBs. This conclusion is supported by studies that show that the local environments around ULXs tend have blue optical colors (Swartz, Tennant, & Soria 2009; Smith et al. 2012). The most extreme ULXs, however, with $L_X \geq 10^{41}$ erg s^{-1} (Farrell et al. 2009; Sutton et al. 2011, 2012), may be intermediate mass black holes, since black holes with masses less than 80 $M_\odot$ are not expected to produce such high luminosities (Zampieri & Roberts 2009; Belczynski et al. 2010; Swartz et al. 2011; Ohsuga & Mineshige 2011).

In order to better understand star formation in hinge clumps, we have searched the archives of the Hubble Space Telescope (HST) and the Chandra X-ray telescope for available images of a sample of hinge clumps. In Section 2 of this paper, we define our sample of hinge clumps and describe the available datasets. Along with the HST and Chandra data, we also include UV images from the Galaxy Evolution Explorer (GALEX) telescope, infrared images from the Spitzer telescope and the Two Micron All Sky Survey (2MASS), ground-based broadband optical images from the Sloan Digitized Sky Survey (SDSS), and published Hα maps. In Section 3, we describe the photometry. We provide approximate star formation rates for the clumps in Section 4. In Section 5, we discuss UV/IR colors for the clumps, and in Section 6, we present the X-ray/UV/IR colors of the clumps. In Section 7 we compare with population synthesis models, and in Section 8 we compare the X-ray luminosities of the clumps with their star formation properties. Conclusions are presented in Section 9. In an Appendix, we describe the individual galaxies in the sample and their morphologies, and provide a detailed discussion of the intense star formation regions within the Antennae galaxies.

2. Sample and Data

2.1. Sample Selection

To study extra-nuclear star formation in interacting galaxies, we have obtained GALEX UV and Spitzer infrared images of three dozen nearby pre-merger interacting galaxy pairs selected from the Arp (1966) Atlas (the 'Spirals, Bridges, and Tails' (SB&T) survey; Smith et al. 2007; 2010). We expanded this search to include other Arp pre-merger pairs with available archival GALEX and Spitzer images (Struck & Smith 2012). We also searched the literature for non-Arp systems with similar morphologies and suitable Spitzer and GALEX images. We identified knots of star formation in these systems by visual inspection of the 8 μm Spitzer images, classifying them as either tidal or disk regions. In a later paper, we will investigate the statistical properties of the full sample of star forming regions. In the current paper, we focus on several systems out of this larger sample that contain prominent hinge clumps, with ample data to allow their detailed study.

We define a hinge clump as a discrete knot of star formation near the base of a tidal tail. To define the 'hinge region', we draw a line from the center of the galaxy through the base of the tail, out to approximately twice the radius of the disk. At right angles to this line in the direction of the spiral of the tail, we draw a second line out from the center of the galaxy, again extending out to approximately twice the radius of the disk. The

portion of the tail that lies within this pie slice defines the hinge region. The choice of 90 degrees here is motivated by the analytical models. In tidally perturbed systems, in alternate quadrants of the galaxy material either gains or loses orbital angular momentum. In the former case the material is flung out in tails, which can commonly form sharp outer/inner edge caustics. In the latter case, disk material compresses, making the light falloff much steeper, if not actually a sharp edge. The meeting point of these two 'sharpened' edges often appears as a cusp point in tailed galaxies. In the models, most of the strong wave overlaps occur within 90 degrees of the base of the tail.

In the current paper, we focus on five systems hosting hinge clumps with high quality multi-wavelength data available (Table 1). To be included in this study, we required the system to have both Spitzer 24 μm and GALEX near-UV images available, as well as either HST or Chandra images. The total number of hinge clumps in the sample is 12, as some of these systems contain more than one hinge clump. All of these hinge clumps are bright, exceeding a S/N of 25 above the surrounding light in either 24 μm or the NUV. Some of the hinge clumps in our sample show up brightly in both the UV and the mid-infrared. Others are bright in the mid-infrared but with little observed UV or with the UV peak offset from that in the mid-infrared. In these cases, we use the mid-infrared peak as the assumed center of the hinge clump. These selection criteria limit the current sample to hinge clumps that are relatively young and luminous; older and fainter regions may be missed by these requirements. Other candidates will be discussed in a later paper.

We provide detailed descriptions of the morphologies of these galaxies in the Appendix to this paper. In the Appendix, we also provide a discussion of numerical and analytical models of the interactions, when available. For four of the five systems, numerical simulations that approximately reproduce the large-scale structure of the galaxies have been published. In addition, for three systems (Arp 82, Arp 240, and Arp 256) we have identified analytical models from Struck & Smith (2012) that approximately match the morphologies of the galaxies. These models are displayed in the Appendix, and compared with the available images. These models suggest that the hinge mechanism, i.e., intersecting caustics, may be responsible for the strong star formation in these regions. The morphologies of the two remaining systems (Arp 270 and NGC 2207) are more complex, and do not match any of the analytical models in Struck & Smith (2012). We include them in our sample because of the availability of high quality data and the existence of high S/N clumps of star formation in the hinge region, however, it is unclear whether the star formation in these clumps is triggered by the same mechanism as the other regions. This issue is discussed further in the Appendix.

Throughout this paper we use distances from the NASA Extragalactic Database (NED[1]), assuming $H_0 = 73$ km s^{-1} Mpc^{-1} and accounting for peculiar velocities due to the Virgo Cluster, the Great Attractor, and the Shapley Supercluster. These distances range from 29.0 Mpc for Arp 270 to 109.6 Mpc for Arp 256 (Table 1).

We compare these hinge clumps to star forming regions within other interacting galaxies, including the Antennae galaxies, as well as the normal spiral galaxy NGC 2403. The available data for these galaxies are discussed further in Section 3.4.

2.2. Spitzer/GALEX/SDSS/Hα/2MASS Datasets

Of the five systems in Table 1, all have GALEX near-UV (NUV) images available and two also have GALEX far-UV (FUV) images. All five have both Spitzer near-infrared (3.6 μm and 4.5 μm) and mid-infrared (5.8 μm, 8.0 μm, and 24 μm) images available. All but one have ground-based SDSS ugriz images available.

The GALEX FUV band has an effective wavelength of 1516 Å with a full width half maximum (FWHM) of 269 Å, while the NUV band has an effective wavelength of 2267 Å and FWHM 616 Å. The GALEX images have 1.″5 pixels, and the point spread function has a FWHM of $\sim 5''$. The Spitzer FWHM spatial resolution is $1.''5 - 2''$ for the 3.6 μm $-$ 8 μm bands, and $\sim 6''$ at 24 μm. The 3.6 μm $-$ 8 μm images have 0.″6 pixel^{-1}, while the 24 μm images have 2.″45 pixel^{-1}. The SDSS pixels are 0.″4, and the SDSS FWHM spatial resolution is typically about 1.″3. The SDSS u, g, r, i, and z

[1] http://ned.ipac.caltech.edu

filters have effective wavelengths of 3560 Å, 4680 Å, 6180 Å, 7500 Å, and 8870 Å, respectively. For more details about the Spitzer, GALEX, or SDSS observations see Smith et al. (2007), Smith et al. (2010), and Elmegreen et al. (2006).

We also obtained copies of published Hα maps for all of the hinge clump systems. These include Hα images of Arp 240 and Arp 256 (Bushouse 1987), Arp 82 (Hancock et al. 2007), Arp 270 (Zaragoza-Cardiel et al. 2013), and NGC 2207 (Elmegreen et al. 2001, 2006). The pixel sizes in these Hα images range from 0.″2 to 0.″595. When necessary, we registered these images to match those at other wavelengths.

We also utilize near-infrared J, H, and K_S (1.235 μm, 1.662 μm, and 2.159 μm) images of these galaxies from the 2MASS survey (Skrutskie et al. 2006). These images have 1.″0 per pixel. Some of the hinge clumps are visible as discrete sources on the 2MASS images. The 2MASS seeing was typically FWHM 2.″5 − 3.″4 (Cutri et al. 2006).

2.3. Hubble Space Telescope Datasets

To study the morphology of these star forming regions at higher resolution, we have searched the HST archives for suitable images. Of our sample, four systems have suitable HST images available that cover the hinge clumps. These galaxies and their HST datasets are listed in Table 2. Together, these four systems host a total of eight hinge clumps.

As can be seen in Table 2, a variety of instruments and filters were used for the HST observations. The data includes images obtained with the Wide Field Planetary Camera (WFPC2), the Advanced Camera for Surveys (ACS), the Wide Field Camera 3 (WFC3), and the Near-Infrared Camera and Multi-Object Spectrometer (NICMOS). Bandpasses available include the far-UV F140LP filter, the near-infrared F160W filter (H band), as well as a range of optical bands. The data that we used was obtained from the Hubble Legacy Archive[2]. The WFPC2 images have a pixel size of 0.″1, while the pixel size for the ACS F140LP FUV images is 0.″025. The ACS optical and the NICMOS F160W images have 0.″05 pixel sizes, while the WFC3 F160W image has 0.″09 pixels.

[2]http://hla.stsci.edu/

2.4. Chandra Telescope Data

To investigate stellar feedback and evolution in these regions, we searched the Chandra archives for suitable datasets. We found archival Chandra images of four interacting systems containing a total of eleven hinge clumps (Table 3).

3. Photometry

3.1. Spitzer, GALEX, SDSS, Hα, and 2MASS Photometry

From the Spitzer, GALEX, SDSS, Hα, and 2MASS images, we extracted aperture photometry of the sample hinge clumps using the Image Reduction and Analysis Facility (IRAF[3]) *phot* routine. We used a 5″ radius aperture, which is a compromise between our desire to study detailed regions within the galaxy and the limiting spatial resolution of the GALEX and Spitzer 24 μm images. This aperture corresponds to 0.70 kpc to 2.7 kpc at the distances of these galaxies. We used a sky annulus with the mode sky fitting algorithm, an inner radius of 6″ and an outer radius of 12″.

Aperture corrections were determined for each of the GALEX images by determining the counts within 5″ and 17″ radii for three to eight moderately bright isolated point sources in the field. These values are tabulated in Table 4. For the Spitzer images, we used aperture corrections from the IRAC and MIPS Data Handbooks. No aperture corrections are needed for the SDSS images. We also did not do aperture corrections for the 2MASS data, as these corrections are expected to be small for photometry with 5″ radii (Cutri et al. 2006). They are also expected to be small for the Hα images.

When necessary, the Hα luminosities have been approximately corrected for the nearby [N II] lines in the filter. We assume a 30% calibration uncertainty for the Hα images in addition to the statistical uncertainties. We calculated Hα equivalent widths for the clumps using the SDSS r band flux for continuum, approximately correcting this flux for contamination by Hα. For most of the clumps, this correction is only 7% − 10%; it is ∼30% for Arp 82-1, Arp 240-3, and Arp 270-4. For NGC 2207, for the Hα continuum we extrapolated be-

[3]http://iraf.noao.edu

tween the HST F555W and F814W bands.

We corrected the SDSS photometry for Galactic reddening as in Schlafly & Finkbeiner (2011), as provided by NED. The GALEX photometry was corrected for Galactic reddening using the Cardelli, Clayton, & Mathis (1989) attenuation law. The final photometry is given in Tables 5 and 6.

3.2. HST Photometry

The HST morphologies of these hinge clumps are often quite remarkable, with a luminous central source embedded in a row of fainter clusters. These linear structures are quite different from the more clustered and amorphous groupings of star clusters seen in HST images of many other galaxies, for example, in the disk of M51 (Bastian et al. 2005). The morphologies of the individual systems are discussed in more detail in the Appendix.

Using the IRAF *phot* routine we extracted magnitudes for the central sources in the various HST bands using apertures of 0.″15 radii, and sky annuli with inner radii of 0.″15 and outer radii of 0.″30. When necessary, we adjusted the registration of the images obtained with different filters to match. We applied aperture corrections as in Holtzman et al. (1995), Sirianna et al. (2005), Dieball et al. (2007), the NICMOS Instrument Handbook, and the WFC3 Instrument Handbook. We corrected the HST photometry for Galactic extinction using the same method as for the GALEX and SDSS photometry. The final photometry is given in Table 7.

The absolute I magnitudes of the central sources in the hinge clumps[4], uncorrected for internal extinction, range from $M_I = -12.2$ to -16.5. Young unobscured clusters typically have V − I colors of −0.4 to 0.7 (e.g., Chandar & Rothberg 2010), so most of these sources are more luminous than typical super-star clusters in interacting galaxies, defined to have absolute V magnitudes $M_V \leq -11$ (e.g., Larsen 2000). If these sources are individual star clusters, they would lie near the top of the luminosity function of super-star star clusters (e.g., Gieles 2010). The most luminous of these objects are comparable in luminosity to the most massive star cluster in the Antennae galaxies, which lies in an intense starburst in the 'overlap' region between the two galaxian disks. This Antennae cluster has $M_V \sim -15.4$ after correction for internal extinction (Whitmore et al. 2010).

The sources in these hinge clumps are more luminous than many nuclear star clusters, for example, the nuclear star clusters in low luminosity spirals have $M_B \sim -10$ and $M_I \sim -11$ (Matthews et al. 1999). Most nuclear star clusters in late-type spirals have absolute I magnitudes between −10 to −14 (Böker et al. 2004), thus the central objects in our hinge clumps are as luminous as or more luminous than many nuclear star clusters.

The sizes of the sources at the centers of the hinge clumps are also quite large, with diameters of 40 pc to 100 pc (see the Appendix). This is much larger than the typical sizes of ∼3 pc for most luminous young star clusters (e.g., Larsen 2004). In the Appendix of this paper, we compare the hinge clumps to HST images of knots of star formation in the Antennae galaxies, smoothed to the same effective resolution as the hinge clumps. We conclude that, if the Antennae were at the distance of the hinge clumps, multiple star clusters would appear blended together, creating larger sources similar in size to those seen in the hinge clumps. Thus we conclude that the large sizes we measure for the central regions of the hinge clumps are likely the consequence of the blending of multiple clusters closely packed together in a complex, rather than a single large cluster.

We also extracted larger-aperture photometry of these hinge clumps from the HST data (Table 8), using 5″ apertures to match those used for the GALEX, Spitzer, SDSS, Hα, and 2MASS photometry given in Tables 1 and 2. In most cases, we used sky annuli with 6″ inner radii and 12″ outer radius, with the mode sky fitting algorithm. For the Arp 82 images, where the clump is near the edge of the field of view, we used a 9″ outer radius. For the ACS F140LP (FUV) images and the NICMOS F160W (H band) images, which have smaller fields of view, we used an annulus with an inner radius of 5″ and an outer radius of 6″. No aperture corrections were needed for the large aperture HST photometry.

Comparison of Table 2 to Table 3 shows that

[4]These magnitudes and those given in the Appendix are in the Johnson system, using the approximate conversions given in the WFPC2 Photometry Cookbook.

the central source within these hinge clumps provides only a small percentage of the total light coming from the hinge clump. The percentage coming from the central source increases with decreasing wavelength. In the F140LP FUV filter, the percentages range from 2.6% to 6.0%, with a median of 3.5%. For the F435W filter, the percentages range from 1.1% to 5.2%, with a median of 2.2%. For the F814 filter, the percentages range from 0.4% to 3.6%, with a median of 1.0%. The lowest percentages are found for the near-infrared F160W filter, ranging from 0.15% to 1.8%, with a median value of 0.7%. This trend suggests that the stars in the central source are younger on average than the stars in the clump as a whole. This suggest that, as with the regions within the disk of Arp 284 studied by Peterson et al. (2009), the hinge clumps contain luminous 'jewels' of young stars embedded in a more extended 'crown' of older stars.

3.3. Chandra X-Ray Spectra and Luminosities

We have detected copious X-rays from eight of the eleven hinge clumps with archival Chandra data available. In five of these clumps, the X-ray emission is well-resolved with Chandra. In one clump (clump 3 in Arp 240W), the x-ray emission is point-like, in a second it appears point-like but may be marginally resolved (clump 1 in Arp 270), while in a third (clump 4 in Arp 240W), there is a point-like hard component superimposed on an extended soft component. The X-ray morphologies of the individual sources are discussed further in the Appendix of this paper.

We extracted X-ray fluxes for these clumps, and used Cash statistics to analyze their X-ray spectra. No background flares were present in the data, so no filtering was needed. The X-ray spectra are generally soft and in most cases appear dominated by thermal emission (Figure 1). In Table 9, we provide the observed $0.3 - 8$ keV flux for the central X-ray source, along with a rough estimate of its size and its coordinates.

Clump 1 in Arp 240W has an X-ray spectrum consistent with a thermal plasma. Clump 2 is also probably thermal plasma, but has too few counts to strongly constrain the parameters. Although clump 3 in Arp 240W is unresolved with Chandra, its X-ray spectrum is intrinsically soft but appears highly absorbed, consistent with a hot plasma (for example, a compact starburst region with diameter ≤ 300 pc or a disk blackbody), rather than a power-law spectrum. The point source in clump 4 in Arp 240W has a very hard spectrum, with 80 counts between 1.2 and 7 keV, and only 2 counts $\leq$ 1.2 keV, and may be very absorbed (see Figure 1). The spectrum can be fit with a power law with a photon index $\gamma = 2.7 \pm \frac{1.0}{0.8}$. Clump 5, at the base of the southern tail in Arp 240E, is extended with a thermal spectrum. The point source in clump 1 of Arp 270 may also be a highly absorbed thermal spectrum, but this is not well-constrained.

We are not able to provide strong constraints on the absorbing hydrogen column density of any of these sources based on the X-ray spectra itself. We therefore estimated the absorption using the $L_{24}/L_{H\alpha}$ ratios. These corrections and the corrected luminosities are discussed at length in Section 7.3. To match the large-aperture GALEX/SDSS/Spitzer/HST photometry, we also obtained X-ray luminosities within a $5''$ radius aperture. In most cases, these are less than twice that of the central source.

3.4. Photometry of Comparison Systems

To put these hinge clumps into perspective, we compare them to star forming regions in other galaxies. We focus in particular on two comparison systems which have high quality X-ray data available in addition to UV/optical/IR images: the Antennae galaxies and the normal spiral galaxy NGC 2403.

For the Antennae, we use the $4\farcs5$ radius (530 pc) Spitzer, GALEX, and ground-based Hα photometry of 34 positions provided by Zhang, Gao, & Kong (2010). Most of these positions were selected based on peaks in the 24 μm map, although three were selected based on GALEX UV sources.

To augment this UV/optical/IR photometry, we used archival Chandra data for the Antennae galaxies. We combined six Chandra observations of the Antennae (ObsID 700479/80/81/82/83) taken in the FAINT mode, removed flares with a sigma clipping method (2.5 σ), giving a total of 329 ksec of observations. This Chandra data has been used in numerous earlier studies of the Antennae (e.g., Fabbiano et al. 2001, 2004;

Zezas & Fabbiano 2002; Zezas et al. 2002a,b, 2006), with the diffuse X-ray emission in the Antennae previously being studied by Metz et al. (2004) and Brassington, Ponman, & Read (2007). We extracted X-ray fluxes for the 34 Zhang, Gao, & Kong (2010) regions, using 4.″5 (530 pc) radius apertures. In the Appendix of this paper, we provide a detailed description of the overlap region of the Antennae, including its X-ray spectra, for comparison to the hinge clumps.

We also compare the hinge clumps to star forming regions within the normal spiral galaxy NGC 2403. For the star forming regions in NGC 2403, we used IRAF to extract Spitzer and GALEX photometry from archival data using the same positions and apertures as used by Yukita et al. (2010) to measure the diffuse X-ray emission. These apertures have radii of 7.″3 − 13.″8, corresponding to 110 pc to 210 pc. For this photometry, we used background annuli with inner and outer radii of 13.″8 and 20.″0, respectively, and the mode sky fitting algorithm. We repeated this process for narrowband Hα and off-Hα red continuum images of NGC 2403 from van Zee et al. (2013, in preparation).

In Section 5 of this paper, we also compare the UV/optical/IR colors of the hinge clumps with published values for star forming regions within other strongly interacting galaxies as well as regions within the Magellanic Clouds.

4. Star Formation Rates

The Hα luminosities for some of the hinge clumps are very high (Table 6). Of our twelve hinge clumps, nine have observed $L_{H\alpha} > 10^{40}$ erg s^{-1} and six have $L_{H\alpha} > 10^{41}$ erg s^{-1}. For comparison, 30 Doradus in the Large Magellanic Cloud has an observed $L_{H\alpha}$ of only 5×10^{39} erg s^{-1}, and the giant H II region complex NGC 5461 in M101 has an observed $L_{H\alpha} \sim 1.5 \times 10^{40}$ erg s^{-1} (Kennicutt 1984).

To complement the Hα luminosities, in Table 10 we provide monochromatic luminosities (νL_ν) of the hinge clumps in the NUV and 24 μm bands. Six of our 12 hinge clumps have L_{NUV} larger than all ten of the TDGs in the SB&T sample (Smith et al. 2010). Seven of the clumps have $L_{24} \geq 6 \times 10^{42}$ erg s^{-1}. For context, out of a sample of 26 normal spirals, only four have *total* 24 μm luminosities in this range (Smith et al. 2007). The entire 24 μm luminosity for the Antennae is 2×10^{43} erg s^{-1}, and for the starburst galaxy Arp 284 it is 3×10^{43} erg s^{-1} (Smith et al. 2007).

In Table 10, we also provide two estimates of the star formation rates (SFRs) of the clumps. First, we use the equation SFR ($M_\odot$ yr^{-1}) = $5.5 \times 10^{-42}[L_{H\alpha} + 0.031\ L_{24}]$ (erg/s), where the 24 μm luminosity L_{24} is defined as νL_ν. This relationship was found for H II regions in nearby galaxies assuming a Kroupa initial mass function (Calzetti et al. 2007; Kennicutt et al. 2009). We make a second estimate of the SFR from the NUV luminosity first correcting for extinction using $L_{NUV}(\mathrm{corr}) = L_{NUV} + 2.26 L_{24}$ and then using the relation $\log(\mathrm{SFR}) = \log(L_{NUV}(\mathrm{corr})) - 43.17$, where $L_{NUV} = \nu L_\nu$ (Hao et al. 2011; Kennicutt & Evans 2012). The two methods agree reasonably well (Table 10). There is a large range in the inferred SFR for the hinge clumps in our sample, from fairly low values (0.02 $M_\odot$ yr^{-1} for Arp 270-1) to very high values. Seven of the 12 hinge clumps have estimated SFRs greater than 1 $M_\odot$ yr^{-1}, with the highest being Arp 240-5, with a rate of 9 $M_\odot$ yr^{-1}. For the two methods of estimating SFR, using global fluxes we calculated the total SFR for the parent galaxies of the target hinge clumps and compared with the SFR for the hinge clump itself. The percent of the total SFR from the galaxy due to the hinge clump ranges from 1% in Arp 270-1 and Arp 270-2 to 56% in Arp 240-5 (Table 10).

These estimates of SFR are very approximate, as these formulae were derived assuming constant star formation rates over the last ∼10 − 100 Myrs (see Kennicutt & Evans 2012), while the clumps have probably undergone recent bursts of star formation. In spite of the uncertainties, however, these numbers aid comparison to other studies, which frequently quote SFRs for both individual knots of star formation within galaxies (e.g., Boquien et al. 2007, 2009b, 2011; Kennicutt et al. 2007; Cao & Wu 2007; Beirão et al. 2009; Pancoast et al. 2010) as well as galaxies as a whole (e.g., Kennicutt & Evans 2012).

For comparison to the hinge clumps, we calculated SFRs for the Antennae regions using the two methods described above. In these calculations, we assume a distance of 24.1 Mpc to the

Antennae[5]. The most intense star formation in the Antennae is occuring in regions 3 and 4 from the Zhang, Gao, & Kong (2010) study, which lie in the overlap region. For these regions, the implied SFRs are $1 - 2$ $M_\odot$ yr^{-1}. Several of our hinge clumps exceed these rates (see Table 10). Summing over all of the regions in the Antennae, we find a total SFR for the Antennae of $9 - 12$ $M_\odot$ yr^{-1} for the two methods.

Although several of these hinge clumps have very high star formation rates, their Hα equivalent widths (Table 6) are not particularly high, compared to those of H II regions within other galaxies (e.g., Cedres, Cepa, & Tomita 2005; Boquien et al. 2009a; Popping, Pérez, & Zurita 2010; Sanchez et al. 2012). This suggests that the hinge clumps contain a wide range of stellar ages and possibly considerable underlying older stellar population. The areas covered by our hinge clump apertures are larger than typically used for Hα photometry of individual H II regions in nearby galaxies, thus we are likely adding light from surrounding older stars to the continuum flux. Other factors that may affect the Hα equivalent width include extinction variations within the clump, metallicity effects, stellar absorption of Hα, and differences in the initial mass function (IMF).

5. UV/IR Colors

In Figure 2, we plot the [3.6 μm] − [24 μm] colors of the hinge clumps vs. the [8.0 μm] − [24 μm] and NUV − [24 μm] colors. We compare these values with published photometry for star forming regions in several other interacting galaxies. These include knots of star formation within the disks of the Antennae galaxies (Arp 244; Zhang, Gao, & Kong 2010), additional star formation regions in Arp 82 besides the hinge clump (from Hancock et al. 2007), as well as tidal and disk clumps in the interacting galaxies Arp 107 (Smith et al. 2005; Lapham, Smith, & Struck 2013), Arp 24 (Cao & Wu 2007), and Arp 143 (Beirão et al. 2009), along with Arp 105 and Arp 245 (Boquien et al. 2010). In this Figure, we excluded sources that are likely to be foreground/background objects not associated with the galaxies (see Lapham, Smith, & Struck 2013). In the left panel of Figure 2, we also include Spitzer colors for H II regions in the Small and Large Magellanic Clouds (Lawton et al. 2010). In Figure 2, we also compare with star forming regions within the normal spiral galaxy NGC 2403, as discussed in Section 3.4.

As can been seen in Figure 2, there is a range in colors for the hinge clumps, however, on average, the hinge clumps have redder [3.6] − [24] colors (i.e., high $L_{24\mu m}/L_{3.6\mu m}$ ratios) than the other clumps. The 3.6 μm emission from galaxies is generally assumed to be dominated by light from the older stellar population/underlying stellar mass (e.g., Helou et al. 2004), while the 24 μm light is emitted from 'very small interstellar dust grains' (VSGs), heated mainly by UV light from massive young stars (e.g., Li & Draine 2001). Thus a red [3.6] − [24] color implies very obscured star formation, a very young burst, and/or a high young/old stellar mass ratio.

The [3.6] − [24] colors of some of the hinge clumps approach that of the 'overlap' region in the Antennae galaxies (Figure 2). The overlap region corresponds to regions 3 and 4 in the Zhang, Gao, & Kong (2010) Antennae study, with region 4 being more obscured. In particular, the [3.6] − [24] color of the NGC 2207 region is similar to that of regions 3 and 4, and is much redder than the other hinge clumps. The Arp 82 hinge clump and Arp 240 clump 3 are also quite red in this color. This supports the idea that these are young regions.

Figure 2 shows that the [3.6] − [24] color is correlated with [8.0] − [24], with some of the hinge clumps having very red [8.0] − [24] colors. The [8.0] − [24] color is a function of the ultraviolet interstellar radiation field (ISRF), with a stronger ISRF producing a higher 24 μm flux compared to that at 8 μm (i.e., a redder [8.0] − [24] color) (Li & Draine 2001; Peeters, Spoon, & Tielens 2004; Lebouteiller et al. 2011). The 8 μm Spitzer band contains emission from both very small dust grains and polycyclic

[5]As for the hinge clumps, in calculating this distance we assume $H_0 = 73$ km s^{-1} Mpc^{-1} and account for peculiar velocities due to the Virgo Cluster, the Great Attractor, and the Shapley Supercluster. A smaller distance of 13.3 Mpc was found by Saviane et al. (2008) based on the apparent tip of the red giant branch. This latter result was questioned by Schweizer et al. (2008), who find 22.3 Mpc based on a type Ia supernova. They suggest that the 13.3 Mpc estimate was probably due to a misidentification of the red giant branch. For more information, see Tammann & Reindl (2013).

aromatic hydrocarbons (PAHs). PAHs can be excited by non-ionizing photons as well as UV, so the 8 μm emission may be powered in part by lower mass stars (Peeters, Spoon, & Tielens 2004; Calzetti et al. 2007; Lebouteiller et al. 2011). The Small Magellanic Clouds regions have redder [8.0] − [24] colors for a given [3.6] − [24] colors, likely caused by less PAHs in the 8 μm band. Low metallicity dwarfs tend to be deficient in the 8 μm Spitzer band compared to normal spirals (Engelbracht et al. 2005; Rosenberg et al. 2006, 2008; Draine et al. 2007; Wu et al. 2007).

The FUV to infrared ratio has sometimes been used as an indicator of dust reddening (e.g., Boquien et al. 2009a), with redder colors meaning more absorption of the UV by dust. Since some of our hinge clumps do not have FUV images available, we use NUV − [24] as an alternative indicator of extinction. Figure 2 shows that there is a range in extinction for the hinge clumps. In Figure 2, the NUV − [24] color correlates to some extent with [3.6] − [24], but there is considerable scatter. In general, the regions within the Antennae are more obscured than many of the other clumps for the same [3.6] − [24] color, particularly those in the normal spiral NGC 2403. Zhang, Gao, & Kong (2010) region 4, in the overlap region of the Antennae galaxies, is particularly red in NUV − [24].

In the left panel of Figure 3, we plot [3.6] − [24] vs. [3.6] − [4.5] for the hinge clumps and the comparison samples. For spiral galaxies as a whole, both the 3.6 μm and 4.5 μm Spitzer bands are generally assumed to be dominated by starlight, as the global [3.6] − [4.5] colors of spirals are usually close to zero (within 0.1 magnitudes) (e.g., Pahre et al. 2004; Smith et al. 2007). However, low metallicity starburst galaxies sometimes show large excesses in these bands above the stellar continuum, with red [3.6 μm] − [4.5 μm] colors (Smith & Hancock 2009). These excesses may be due to hot dust and/or nebular emission (Brα line emission and/or the nebular continuum). All of these factors are expected to be stronger in younger clumps, while the nebular components will be enhanced in low metallicity systems.

Within interacting galaxies, localized knots of intense star formation sometimes have large excesses above the stellar continuum in the 3.6 μm and 4.5 μm bands, particularly in the 4.5 μm filter (Smith et al. 2008; Zhang, Gao, & Kong 2010; Boquien et al. 2010). In Figure 3 (left), a trend is seen, such that the regions with redder [3.6] − [24] colors are redder in [3.6] − [4.5]. This is consistent with increasing 4.5 μm non-stellar excess with younger stars or higher young/old star ratios. However, there is considerable scatter in this plot. In particular, the Magellanic Cloud regions are redder in [3.6] − [4.5] for the same [3.6] − [24] color compared to the regions within the interacting galaxies (Figure 3). This may be a consequence of lower metallicity. Such an offset is also seen in the global colors of low metallicity dwarfs compared to higher metallicity galaxies (Smith & Hancock 2009).

Interestingly, some of the NGC 2403 regions also lie to the right of the correlation marked by the clumps in the interacting galaxies, in the regime populated by the Magellanic Cloud regions. This may also be a metallicity effect. The red NGC 2403 regions are preferentially found at larger galactic radii. NGC 2403 is a moderate luminosity ($M_B = -18.9$; Moustakas, et al. 2010) late-type (Scd) spiral. The NGC 2403 region with the largest [3.6] − [4.5] color, J073628.6+653349, has a deprojected distance from the nucleus of 6.21 kpc (Garnett et al. 1997). Its oxygen abundance has been determined by the direct electron temperature method to be $\log(O/H) + 12 = 8.10 \pm 0.03$ (Garnett et al. 1997) or $\log(O/H) + 12 = 8.28 \pm 0.04$ (Berg et al. 2013). This is in the range where red [3.6] − [4.5] colors become more common for dwarf galaxies (Smith & Hancock 2009). No metallicities are available for our hinge clumps at present.

In the right panel of Figure 3, we plot the [3.6] − [24] color against the 24 μm luminosity. A rough correlation is seen in this plot, such that the clumps with the highest luminosity tend to be redder. The large scatter in this plot is likely due in part to the fact that the apertures cover different physical sizes in the different galaxies. Note that the NGC 2403 and Magellanic Cloud luminosities are lower on average, due to the smaller areas covered. The LMC and SMC apertures range from 105 pc to 450 pc (Lawton et al. 2010).

6. X-Ray vs. UV/IR Colors

In Figure 4 we plot the observed (uncorrected for dust attenuation) log $L_X/L_{24\mu m}$ against [3.6] − [24] and against NUV − [24], for the hinge clumps with Chandra data available. In this Figure we compare with both the star forming knots in the Antennae as well as the star forming regions within the normal spiral NGC 2403. For the regions in NGC 2403, we used the diffuse X-ray fluxes from Yukita et al. (2010), which were obtained from the Chandra map after bright point sources were removed. This plot shows that the NGC 2403 regions have lower observed $L_X/L_{24\mu m}$ for a given [3.6] − [24] color than either the hinge clumps or the positions in the Antennae. They also have lower [NUV] − [24] values, indicating lower extinction. Some of the hinge clumps lie in the region populated by the Antennae points, while some are lower on this plot. The NGC 2207 clump lies between Antennae overlap regions 3 and 4 in these plots, with large [3.6] − [24] and low observed $L_X/L_{24\mu m}$.

Correcting these X-ray fluxes for dust attenuation is critical, given the large absorbing columns towards some of these regions implied by their red NUV − [24] colors. The correction for dust attenuation is discussed further in Section 7.3.

Two of the hinge clumps with X-ray point sources (Arp 270-1 and Arp 240-4) likely host ULXs, as their X-ray luminosities are very high compared to other regions with similar [3.6] − [24] colors (Figure 4). Alternatively, these regions may contain two or more lower luminosity HMXBs very close together. The third X-ray point source, Arp 240-3, has a location on this plot similar to that of the clumps resolved by Chandra, thus its X-ray emission may be due to a compact young star formation region rather than a ULX. This is consistent with its intrinsically soft X-ray spectrum (Section 3.3).

7. Stellar Population Synthesis Models

7.1. Overview

We compared the large aperture GALEX/SDSS broadband UV/optical colors of these clumps with population synthesis models to determine the ages of their stellar populations and their dust attenuations. We used the large aperture HST photometry as a check on these fits. We did not use the 2MASS near-infrared or Spitzer 3.6 and 4.5 μm fluxes in these fits, although this light may also be dominated by starlight. This point is discussed further in Section 7.2. We obtained a second independent estimate of the stellar age from the Hα equivalent width.

For this analysis we assume a single instantaneous burst. As discussed below, for some of these clumps more than one generation of stars may be present. In these cases, the ages we derive from the single-burst models are a luminosity-weighted average age for the stars in the clump. As in our earlier studies (Smith et al. 2008; Hancock et al. 2009; Lapham, Smith, & Struck 2013), we use the Starburst99 population synthesis code (Leitherer et al. 1999) and include the Padova asymptotic giant branch stellar models (Vazquez & Leitherer 2005). We assume a Kroupa initial mass function and solar metallicity. We integrated the model spectra over the GALEX and SDSS bandpasses, including the Hα line from Starburst99 in the model spectra as well as other optical emission lines, derived using the prescription given by Anders & Fritz-v. Alvensleben (2003) for solar metallicity star forming regions. We used the Calzetti, Kinney, & Storchi-Bergmann (1994) starburst dust attenuation law.

The best-fit ages and dust reddening E(B−V) values from the broadband photometry are given in Table 11, along with uncertainties on these values. These were computed using a chi squared (χ^2) minimization calculation as in our earlier studies. For these fits, we only used the filters with reliable detections; upper limits were ignored. When available, we used the FUV − NUV, NUV − g, u − g, g − r, r − i, and i − z colors for fitting. In calculating the χ^2 values, in addition to the statistical errors, we included additional uncertainties in the colors due to uncertainties in the GALEX aperture corrections (see Table 4) and in background subtraction. To estimate the uncertainties due to background subtraction, we calculated colors using an alternative second sky annulus with an inner radius of 8″ and an outer radius of 14″. To estimate the uncertainties in the best-fit parameters, we used the $\Delta\chi^2$ method (Press et al. 1992) to determine 68.3% confidence levels for the parameters. In Table 11, we provide the reduced χ^2, equal to $\chi^2/(N-2)$, where N is the number of

colors used in the fit.

As can be seen in Table 11, for some of the clumps the fits are quite good. For a few, however, the χ^2 values indicate a very poor fit (e.g., Arp 82, Arp 240-1, Arp 240-3, and especially Arp 256). This suggests that more than one age of stars are present. Two or more bursts of star formation may have occured in the region, or the star formation continued over an extended time period.

We obtain a second independent estimate of the age of the stellar population using the Hα equivalent width and assuming an instantaneous burst. These ages are tabulated in Table 12. Except for regions Arp 240-1, Arp 256-1, Arp 270-1, and Arp 270-3, these ages are younger than the ages derived from the broadband UV/optical fluxes (Table 11). Such differences in derived ages have been found earlier for some knots of star formation in Arp 284 and Arp 107 (Peterson et al. 2009; Lapham, Smith, & Struck 2013), and provide additional support for the idea that these hinge clumps host a range of stellar ages. Ages from Hα equivalent widths tend to be biased towards the younger populations in a region, while the broadband ages are weighted towards the somewhat older stars that sometimes dominate the UV/blue light from star forming regions. The comparison of these two age estimates illustrates the uncertainties in age determinations via population synthesis.

7.2. SED Plots and Near-IR Excesses

In Figures 5 to 7, we plot the large-aperture spectral energy distributions (SEDs) for these clumps, including the GALEX, SDSS, Spitzer, 2MASS, and HST large aperture photometry. On these plots, we overlay the best-fit Starburst99 single-population models from the broadband data. As an indication of the uncertainties in these models, in these figures we also plot models with the best-fit reddening and the best-fit age $\pm$ the 1σ uncertainty in the age. As can be seen from these plots, in some cases a single-burst model does not provide a good match to the SED. For NGC 2207, which lacks SDSS data, we do not provide a best-fit model, however, comparison to the other SEDs shows that it has quite red colors, consistent with high obscuration (see Section 7.3).

As shown in Figures 5 $-$ 7, for some of the clumps the Spitzer 3.6 μm and 4.5 μm fluxes are higher than predicted by the best-fit single-burst models, which do not include dust emission. In some cases, the HST or 2MASS near-infrared fluxes are also higher than expected from our single-burst models. This is additional evidence for two or more generations of stars or ongoing star formation. Alternatively, as noted in Section 5, there may be excess flux in these bands above the stellar continuum due to hot dust or to interstellar gas emissions (see Smith & Hancock 2009).

Instead of instantaneous bursts, a better model of the star formation history in these clumps might be prolonged star formation (continuous for an extended period, then shut off), or an exponentially-decaying star formation rate (e.g., Boquien et al. 2010). As discussed in the Appendix of this paper, regions 3 and 4 in the Antennae galaxy each host stars with a range of ages; our hinge clumps, which cover even larger physical sizes than the Antennae photometry, may also contain a range of stellar ages. As an approximation, in Lapham, Smith, & Struck (2013) we explored models with two instantaneous bursts for fitting clumps of star formation within Arp 107. These provide better fits to the SEDs than single bursts, but we were unable to constrain the parameters of the fit well, as we were able to find multiple models with very different parameters that fit the data equally well. In general, adding more parameters to the fitting routine by allowing more than one stellar age increases the uncertainties in the derived parameters. Thus in this work, we focus on single-burst models, and emphasize that the derived ages are luminosity-weighted stellar ages, averaged over the timescale of the burst, and the star formation was likely prolonged rather than truly instantaneous.

It is also possible to include the mid-infrared photometry in the population synthesis modeling (e.g., Noll et al. 2009; Boquien et al. 2010). However, this also adds additional parameters to the model, including the dust properties and the location of the dust relative to the stars. Thus in this work we derive ages from only the UV/optical data.

7.3. Attenuation

In Table 11, we provide the E(B−V) estimates determined from the broadband Starburst99 modeling. We obtained a second independent estimate of the absorption using the ratio of the 24 μm luminosity to Hα luminosity (Table 12). For this calculation, we used the empirically-determined relationship between the absorption in the Hα emission line and the 24 μm emission obtained by Kennicutt et al. (2007) for star forming regions within M51: $A_{H\alpha} = 2.5 \log[1 + 0.038 L_{24}/L_{H\alpha}]$. As noted by these authors, there is considerable scatter in this relation, and for a given star forming region the true relation likely depends upon the geometry, the stellar types, and the age. In the hinge clumps, we expect an even larger scatter in the relationship, as we are likely averaging over a range of extinctions within the beam. We converted from $A_{H\alpha}$ to hydrogen column density using $A_{H\alpha} = 0.82 A_V$ and the Calzetti et al. (2000) starburst total to selective attenuation ratio $R_V = A_V/E(B-V) = 4.05$.

For some of the clumps, the absorption derived from $A_{H\alpha}$ agrees reasonably well with that obtained from the broadband photometry. For others, the Hα-derived estimates are higher than that inferred from the broadband photometry. This difference may be caused by a range of ages and extinctions in the clumps, with the younger stars being more obscured. In starburst galaxies, the ionized gas tends to be more obscured than the starlight on average (e.g., Calzetti 2001). For the region in NGC 2207, our estimate of $A_V = 4.1$ from $L_{24}/L_{H\alpha}$ (Table 12) is consistent with the Kaufman et al. (2012) limit of $A_V \leq 4.9$ determined from the ratio of the 6 cm flux to that in Hα.

As mentioned in Section 3.3, we are not able to determine X-ray absorptions directly from the Chandra data itself. We therefore correct the X-ray data for absorption using column densities obtained from the $L_{24}/L_{H\alpha}$ ratio, as it is likely more valid for the ionized gas than values obtained from broadband photometry. We first converted from E(B−V) to hydrogen column density using $N_H(cm^{-2}) = 5.8 \times 10^{21} E(B-V)$ (Bohlin, Savage, & Drake 1978). These estimates range from $N_H = 1 - 6 \times 10^{21}$ cm^{-2} (see Table 12). We emphasize that these estimates are quite uncertain, since the X-ray emitting gas may be less obscured than the Hα-emitting ionized gas within H II regions. However, these estimates are similar to the absorbing column densities found by Mineo, Gilfanov, & Sunyaev (2012b), who fit X-ray spectra of the global diffuse X-ray emission of a sample of nearby late-type star forming galaxies. Obtaining higher quality X-ray data for our hinge clumps would be very valuable to better constrain the X-ray absorption.

Using these estimates of the absorbing column, we next determined the ratio of the attenuation in the 0.3 − 8 keV X-ray band to the hydrogen column density A_X/N_H using the *wabs* routine in the XSPEC[6] software (this uses the Wisconsin absorption cross-sections, e.g., Morrison & McCammon 1983). The A_X/N_H ratio depends upon both the X-ray spectrum and the hydrogen column density. For this calculation, we assumed a 0.3 keV thermal spectrum, thus A_X/N_H varies between 7.19×10^{-22} mag cm^2 for $N_H = 3 \times 10^{20}$ cm^{-2} and $A_X/N_H = 2.73 \times 10^{-22}$ mag cm^2 for $N_H = 2 \times 10^{22}$ cm^{-2}.

These corrections have been applied to the observed X-ray fluxes. In Table 9, we provide absorption-corrected X-ray luminosities for each hinge clump. We provide both the luminosity of the central source, as well as luminosities within the larger 5″ radius aperture, assuming the same correction factor for both. These corrections are generally multiplicative factors of 2 − 5, with larger correction factors for the two most obscured regions Arp 240-5 and NGC 2207 (factors of 9 and 13, respectively). We emphasize that these corrected luminosities are quite uncertain due to uncertainties in both the correction method and in the fluxes themselves.

The absorption-corrected X-ray luminosities L_X (0.3 − 8 keV) of the eight detected hinge clumps (Table 9) are all greater than 10^{39} erg/s, with seven greater than 10^{40} erg/s. For the three hinge clumps that were undetected by Chandra, we provide upper limits in Table 9 assuming the reddening from the $L_{24}/L_{H\alpha}$ ratio.

The most X-ray luminous region in Table 9 is the point source in clump 4 of Arp 240W, which has a corrected 0.3 − 8 keV luminosity of $\sim 2 \times 10^{41}$ erg s^{-1}. The absorption correction for

[6] http://heasarc.gsfc.nasa.gov/docs/xanadu/xspec/index.html

this source may be overestimated by the above method, if the source has a intrinsically hard spectrum. However, even without any correction at all, the luminosity of this source is high, 5×10^{40} erg s^{-1}. Obtaining higher S/N X-ray spectroscopy of this source would be very valuable, to better determine the absorbing column and therefore the intrinsic luminosity. At a luminosity of $\sim 2 \times 10^{41}$ erg s^{-1}, this would be one of the most luminous ULXs known, and therefore a possible intermediate mass black hole.

7.4. Stellar Masses

For both methods of determining ages and extinctions, we estimated stellar masses for the clumps (Tables 11 and 12). As expected, the masses derived using the Hα equivalent widths are sometimes lower than those obtained from the broadband photometry, since the inferred ages are younger. We note that stellar masses derived by scaling directly from the K and 3.6 μm photometry (e.g., Bell & de Jong 2001; Bell et al. 2003; Into & Portinari 2013) are considerably larger (factors of $2 - 25$ times larger) than the masses obtained from individual fitting of the UV/optical broadband photometry. These scaling factors are intended for galaxies as a whole rather than individual star forming regions within galaxies, and, as discussed by Gallazzi & Bell (2009), they may over-estimate the stellar mass in systems undergoing recent bursts. Even when population synthesis fitting is done, the stellar masses are quite uncertain (up to a factor of 5; Smith et al. 2008).

8. L_X vs. Star Formation Properties

8.1. L_X/SFR Ratios: The Hinge Clumps, Antennae, and NGC 2403

In Table 12 we provide $L_X/L_{H\alpha}$ and L_X/SFR ratios for each hinge clump, corrected for extinction using the Hα/24 μm-derived values. For these calculations, we use the X-ray fluxes within a 5″ radius. Two of the hinge clumps (Arp 240-4 and Arp 270-1) have much higher values than the rest, supporting the idea that they are ULXs. For the remaining clumps, this table shows that the X-ray luminosity is not perfectly correlated with SFR, since there is a scatter of about a factor of four in these ratios.

For the Antennae and NGC 2403 we calculated L_X/SFR ratios using the same procedure. As with the hinge clumps, for both the Antennae and NGC 2403 it is difficult to constraint the internal extinction from the X-ray spectra alone (e.g., Metz et al. 2004; Yukita et al. 2010). We therefore estimate the dust absorption within these regions using the 24 μm and Hα fluxes within our apertures, as we did for the hinge clumps. For the Antennae these range from $A_V = 0.67$ to 3.23, with region 4 having the highest value. For the NGC 2403 regions, the implied absorption is much smaller than for the Antennae and the hinge clumps, with A_V between 0.08 and 0.50.

Excluding the regions with bright X-ray point sources, the median extinction-corrected L_X/SFR for the Antennae areas is 5.7×10^{39} (erg/s)/($M_\odot$ yr^{-1}) using the Hα+24 μm estimate of SFR. For the NUV+24 μm method, the median L_X/SFR is 8.3 $\times 10^{39}$ (erg/s)/($M_\odot$ yr^{-1}) for the Antennae regions. These are similar to the ratios for the non-ULX hinge clumps (Table 12).

For NGC 2403, the absorption-corrected L_X/SFR ratios have a median value of 6×10^{38} (erg/s)/($M_\odot$ yr^{-1}) for the Hα+24 μm method and 4×10^{39} (erg/s)/($M_\odot$ yr^{-1}) for the NUV+24 μm method. The latter value agrees reasonably well with those of the hinge clumps, while the ratio determined using the Hα+24 μm method is somewhat lower.

8.2. L_X/SFR Ratios From Other Studies

For a sample of nearby spirals and irregulars, Mineo, Gilfanov, & Sunyaev (2012b) extracted the diffuse X-ray emission and compared with the SFR. Their best-fit value for the ratio of the extinction-corrected $0.3 - 10$ keV X-ray luminosity from hot gas to the SFR is L(0.3 − 10 keV)/SFR = $(7.3 \pm 1.3) \times 10^{39}$ (erg/s)/($M_\odot$ yr^{-1}). Given their somewhat different definition of SFR, their different energy range, and their different method of correcting for internal extinction, their results are consistent with our values for the hinge clumps (Table 12). They also agree well with our values for the Antennae regions dominated by diffuse X-ray emission (Section 8.1). The Mineo, Gilfanov, & Sunyaev (2012b) ratios are somewhat higher than the mean L_X/SFR of 1.4×10^{39} (erg/s)/($M_\odot$ yr^{-1}) found by Li & Wang (2013) for the coronal X-ray emission from 53 edge-on disk galaxies.

In Smith, Struck, & Nowak (2005), we collated X-ray luminosities, extinction-corrected Hα luminosities, and published ages for 20 H II regions within Local Group galaxies and the nearby galaxies M101 and NGC 4303. Regions with ages $\leq$3 Myrs (before supernovae turn on) show dramatically lower L_X/SFR ratios than older regions. The younger H II regions have a median L_X/SFR of 3.4 $\times$ 10^{36} (erg/s)/($M_\odot$ yr^{-1}). This contrasts sharply with the median value of the rest of the regions of 2 $\times$ 10^{39} (erg/s)/($M_\odot$ yr^{-1}). Our hinge clumps have ratios similar to those of the older H II regions, indicating that supernova activity has begun in the hinge clumps.

In Smith, Struck, & Nowak (2005), we found extended X-ray emission from four H II regions in the primary disk of the interacting pair Arp 284 using Chandra. Using the same conversion as above, for these regions we find L_X/SFR between 8 $\times$ 10^{39} (erg/s)/($M_\odot$ yr^{-1}) and 4 $\times$ 10^{40} (erg/s)/($M_\odot$ yr^{-1}). These are similar to the values for our hinge clumps.

From these comparisons, we conclude that the hinge clumps are producing X-rays at a rate relative to the SFR similar to those of star forming regions in other galaxies.

8.3. HMXBs

The intrinsically soft X-ray spectra of most of the hinge clumps argues that this emission is dominated by hot gas. However, a fraction of the observed X-ray emission may be due to the combined light of multiple unresolved X-ray point sources. For star forming regions, this additional component is likely dominated by HMXBs, as the number of HMXBs in a galaxy is correlated with the SFR (Grimm, Gilfanov, & Sunyaev 2003; Gilfanov, Grimm, & Sunyaev 2004; Persic et al. 2004; Mineo, Gilfanov, & Sunyaev 2012a). Other kinds of X-ray-emitting objects, such as YSOs, hot stars, and low mass X-ray binaries, are expected to be less important to the observed X-ray emission from strongly star forming systems (e.g., Bogdán & Gilfanov 2011; Mineo, Gilfanov, & Sunyaev 2012b). HMXBs are associated with populations with ages between 20 and 70 Myrs (Antoniou et al. 2010; Williams et al. 2013). These ages are consistent with our estimates of the average stellar ages in some of the hinge clumps from the broadband UV/optical photometry. Thus sufficient time may have passed to produce HMXBs in at least some of our hinge clumps.

To estimate the contributions from HMXBs to the X-ray luminosities of the hinge clumps, we use the relation found by Mineo, Gilfanov, & Sunyaev (2012a) for HMXBs in nearby star forming galaxies of L(0.5 $-$ 8 keV)(HMXBs) = SFR $\times$ (2.6 $\times$ 10^{39} erg s^{-1}). As discussed at length by Mineo, Gilfanov, & Sunyaev (2012a), this relation agrees well with relations found by Grimm, Gilfanov, & Sunyaev (2003) and Ranalli, Comastri, & Setti (2003), after conversion to the same energy range and SFR definitions. Excluding the two candidate ULXs, this relation implies that about 15% $-$ 30% of the X-ray light from the hinge clumps comes from HMXBs, with an estimated fraction of 40% for clump 1 in Arp 240. These estimates are very uncertain, as there is a lot of scatter in the SFR-HMXB relation (Mineo, Gilfanov, & Sunyaev 2012a), and this relation was derived by averaging over entire galaxies, thus it is not necessarily appropriate for individual star forming regions. However, it provides a very approximate estimate, which supports our conclusion based on the soft X-ray spectra that in most cases the X-ray emission from these clumps is dominated by radiation from hot gas rather than HMXBs.

As noted earlier, the absorption-corrected X-ray luminosity of clump 4 in Arp 240 (2 $\times$ 10^{41} erg s^{-1}) is higher than expected for HMXBs, thus it may host an intermediate-mass black hole. Alternatively, it may contain multiple luminous HMXBs. Its L_X/SFR of 7 $\times$ 10^{40} erg s^{-1} $(M_\odot/yr)^{-1}$ (Table 12) is more than an order of magnitude higher than that found by Mineo, Gilfanov, & Sunyaev (2012a) for HMXBs in nearby spiral galaxies. If this X-ray emission is due to a collection of HMXBs, this region is either unusually rich in HMXBs per SFR compared to other systems, or its star formation rate was considerably higher in the very recent past. However, our Hα and NUV estimates of star formation rate for this clump agree well (2.8 $M_\odot$ $year^{-1}$ and 2.3 $M_\odot$ $year^{-1}$; Table 10), although Hα and NUV are sensitive to star formation on different timescales ($\sim$10 Myrs and $\sim$200 Myrs, respectively; Kennicutt & Evans 2012). Thus there is no evidence for a dramatic drop in SFR in this region in the $\leq$70 Myrs timescale for HMXB production. The total stellar mass of this clump (2

$\times 10^8$ to 1×10^9 $M_\odot$; Tables 11 and 12) could be produced by a steady rate of $\sim 2 - 3$ $M_\odot$ year^{-1} over ∼200 Myrs, without requiring a significantly higher rate in the recent past, but that steady rate would not be enough to produce such a high HMXB luminosity today.

8.4. ULXs

A related question is whether the hinge clumps host ULXs at the rate expected from their SFRs, where a ULX is defined to be a point source with $L_X \geq 10^{39}$ erg s^{-1}. As noted earlier, most ULXs with luminosities between 10^{39} erg s^{-1} and 10^{41} erg s^{-1} are likely high luminosity HMXBs. Out of our 12 hinge clumps, three host point sources with $L_X \geq 10^{39}$ erg s^{-1}, however, the source in Arp 240-3 has a likely thermal spectrum, and as discussed below, its X-ray emission is probably dominated by hot gas. The other two point sources, Arp 240-4 and Arp 270-1, are candidate ULXs.

To determine whether the frequency of ULXs in hinge clumps relative to the SFR is consistent with those of galaxies as a whole, we compare to our statistical studies of ULXs in normal galaxies (Swartz et al. 2004, 2011) and strongly interacting galaxies from the Arp Atlas (Smith et al. 2012). In those studies, we determined the number of ULXs per far-infrared luminosity L_{FIR} for various samples of galaxies. To compare with these studies, we estimated L_{FIR} for the hinge clumps using the Calzetti et al. (2005) relation between the 8 μm and 24 μm fluxes and the total infrared luminosity L_{IR}, and used the approximate relation between L_{FIR} and L_{IR} of $L_{FIR} = 0.55 L_{IR}$ from Helou et al. (1988).

For all but one of our sample galaxies, the Chandra sensitivity is insufficient to detect all ULXs down to the limiting luminosity of $L_X \geq 10^{39}$ erg s^{-1}. However, the Chandra data for all of our systems have sufficient sensitivity to detect ULXs more luminous than $L_X \geq 10^{40}$ erg s^{-1}. We can compare the number of ULXs above $L_X \geq 10^{40}$ erg s^{-1} with the combined estimated far-infrared luminosity of all of the sample hinge clumps, 2.2×10^{44} erg s^{-1}. We find only one candidate ULX in our hinge clump sample above 10^{40} erg s^{-1}, Arp 240-4. This gives a ratio of the number of ULXs above 10^{40} erg s^{-1} per far-infrared luminosity of $N_{ULX}/L_{FIR} = 4.6 \times 10^{-45}$ (erg s^{-1})$^{-1}$. This is consistent within the uncertainties with the ratios found for spiral galaxies of $N_{ULX}/L_{FIR} = 6.7 \pm ^{2.9}_{2.1} \times 10^{-45}$ (erg s^{-1})$^{-1}$ (Swartz et al. 2004) or $9.4 \pm 2.2 \times 10^{-45}$ (erg s^{-1})$^{-1}$ (Swartz et al. 2011). Interestingly, the Arp sample appears to have a deficiency of ULXs in this luminosity range, with $N_{ULX}/L_{FIR} = 9.6 \times 10^{-46}$ (erg s^{-1})$^{-1}$ (Smith et al. 2012). This may be because the Arp sample includes a number of ultra-luminous infrared galaxies (ULIRGs), which dominate the combined far-infrared luminosity of the sample yet have relatively few ULXs. ULXs may be more obscured in ULIRGs, leading to a deficiency in the observed number of ULXs in this sample; alternatively, hidden AGN may be contributing to L_{FIR} in the ULIRGs (Smith et al. 2012). Hinge clumps appear to be forming $L_X \geq 10^{40}$ erg s^{-1} ULXs at a rate relative to their SFR similar to spirals. They do not appear to be deficient in these ULXs relative to the SFR, in contrast to ULIRGs.

Only for Arp 270 is the Chandra sensitivity sufficient to detect all ULXs down to 10^{39} erg s^{-1}. The combined estimated L_{FIR} for the four hinge clumps in Arp 270 is 1.5×10^{42} erg s^{-1}, giving $N_{ULX}/L_{FIR} = 6.6 \times 10^{-43}$ (erg s^{-1})$^{-1}$ for $L_X \geq 10^{39}$ erg s^{-1}. This is considerably higher than the N_{ULX}/L_{FIR} ratio for spirals of $6.5 \pm 0.7 \times 10^{-44}$ (erg s^{-1})$^{-1}$ (Swartz et al. 2004) or $5.3 \pm 0.5 \times 10^{-44}$ (erg s^{-1})$^{-1}$ (Swartz et al. 2011). This difference may simply be due to small number statistics; alternatively, the candidate ULX in Arp 270-1 may be a background source rather than a true ULX.

In the ULX luminosity range $\geq 10^{39}$ erg s^{-1}, the N_{ULX}/L_{FIR} ratio for Arp systems is similar to that of spirals, $7.6 \pm 1.3 \times 10^{-44}$ (erg s^{-1})$^{-1}$ (Smith et al. 2012). The subset of Arp systems in the Smith et al. (2012) sample that have Chandra sensitivity to 10^{39} erg s^{-1} point sources contains fewer high L_{FIR} systems than the larger Arp sample with Chandra sensitivity to only 10^{40} erg s^{-1}. The 10^{39} erg s^{-1} sample of Arp systems appears similar to spirals in their ULX populations.

8.5. Electron Densities in the Hot Gas

To estimate the electron number density n_e in the hot gas within the hinge clumps, we used the angular extents of the central X-ray source (Table 9) to calculate the volume of X-ray-emitting gas, assuming an ellipsoidal shape with the third axis equal to the average of the other two di-

mensions. For the NGC 2403 regions, we estimated the volume using the radii of the X-ray-emitting regions obtained by Yukita et al. (2010), and assumed a spherical shape. For the Antennae, we estimated angular extents of the diffuse X-ray emission for each region from the co-added Chandra map, assuming an ellipsoidal shape as for the hinge clumps. For each of these regions, we calculated $n_e\sqrt{f}$, where f is the volume filling factor (Table 12). We used standard cooling functions (McKee & Cowie 1977; McCray 1987) and assumed thermal emission with a temperature kT of 0.3 keV. We used the L_X of the central source for these calculations rather than the large aperture luminosity. We emphasize that these estimates of $n_e\sqrt{f}$ are very uncertain, because of uncertainties in the measured angular extent of the X-ray emission which is a function of sensitivity, as well as lack of information about the line-of-sight path length through the ionized region and the three-dimensional geometry of the regions.

8.6. $L_X/L_{H\alpha}$ vs. Other Parameters

In Figures 8, 9, and 10, we plot the extinction-corrected $L_X/L_{H\alpha}$ ratios against the Hα equivalent widths, the hydrogen column densities (determined from the Hα/24 μm ratios), and $n_e\sqrt{f}$. We calculated Hα equivalent widths for the Antennae regions using the Zhang, Gao, & Kong (2010) photometry, interpolating between the HST F555W and F814W fluxes for the red continuum. For the NGC 2403 regions, we used fluxes from the van Zee et al. (2013, in preparation) Hα and off-Hα images to calculate equivalent widths. These agree reasonably well with spectroscopic Hα equivalent widths determined for a few of our NGC 2403 regions by Berg et al. (2013).

Figures 8, 9, and 10 show clear differences between the NGC 2403 regions and the other regions, while the values for the Antennae and hinge clumps overlap. The NGC 2403 equivalent widths are generally larger than those for the Antennae regions and the hinge clumps. In the hinge clumps and in the Antennae regions, the ionized gas may be more obscured relative to the overall starlight, producing smaller observed equivalent widths. Lower metallicity in some of the NGC 2403 regions may also contribute to higher Hα equivalent widths. In addition, the NGC 2403 apertures cover smaller physical areas on the galaxy, closer to the central star formation; more older stars may be included in the larger Antennae and hinge clump apertures. Since both the hinge clumps and the Antennae regions likely contain a range of stellar ages (see Appendix), their Hα equivalent widths are a rough proxy for the luminosity-weighted mean stellar age.

The NGC 2403 regions have lower N_H and $n_e\sqrt{f}$ values than the hinge clumps and Antennae regions. This is expected, as star forming regions in normal galaxies are expected to be less obscured and less dense on average than regions in strongly interacting galaxies.

The NGC 2403 regions also have lower extinction-corrected $L_X/L_{H\alpha}$ ratios than the other regions. This may be due to younger ages on average in the NGC 2403 regions, as suggested by their higher Hα equivalent widths. Very young star forming regions are not expected to host significant supernovae activity, while hot gas may build up with time in older regions with successive generations of star formation. Alternatively, the lower gas number densities and gas column densities towards the NGC 2403 regions may be responsible for their lower relative X-ray emission. The higher the density of the region, the more X-ray production is expected due to a higher particle collision rate. This topic is discussed further in the next section.

8.7. The X-Ray Production Efficiencies

To further investigate these issues, in this section we compare the large-aperture X-ray luminosities with Starburst99 predictions of the rate of mechanical energy injection into the region from hot star winds (ignoring red giant stars) and supernova. The ratio of the absorption-corrected X-ray luminosity to the mechanical luminosity is defined as the X-ray production efficiency (XPE; the fraction of the mechanical luminosity emitted in X-rays). To calculate XPEs it is necessary to have estimates of the extinction and the average stellar age. For this calculation, we use the ages and reddenings derived from the Hα data (Table 12), as these are likely more relevant for the X-ray-emitting hot gas than values obtained from the broadband photometry (Table 11). Using these values and SB99, we derive mechanical energy rates and thus XPEs for the clumps assuming that all of the X-ray light comes from hot

gas and not HMXBs. These XPEs are tabulated in Table 12. Most of the hinge clumps with extended X-ray emission have similar inferred XPEs of ∼0.6%, while Arp 240-1 has a lower value of ∼0.2%.

We emphasize that these XPEs are uncertain for several reasons. First, there is likely a range in both age and attenuation in these clumps, making our estimates of both the mechanical luminosity and the extinction uncertain. Second, the cooling time for the X-ray emitting gas can be quite long, while our determination of the XPE uses an instantaneous estimate of the mechanical luminosity. Ideally, in calculating XPE one should average the rate of mechanical energy injection over an extended time period, taking into account the variation of the star formation rate with time along with gas cooling rates. Given these caveats, it is unclear how significant the variations in XPEs from one hinge clump to another are.

However, even taking these caveats into account, two of the X-ray point sources, Arp 270-1 and Arp 240-4, have very high derived values of XPE (8.0% and 3.2%, respectively). This again suggests that these two regions host ULXs rather than hot gas, in spite of the possible thermal X-ray spectrum for Arp 270-1. The third X-ray point source, Arp 240-3, has an XPE similar to that of the clumps with diffuse X-ray emission, suggesting that its X-ray emission is dominated by light from hot gas.

For many of the clumps, the older ages obtained from the broadband photometry (Table 11) are inconsistent with the X-ray fluxes, if the X-ray emission is only due to hot gas, the burst is instantaneous, and the hot gas cools quickly. A dramatic drop-off in the mechanical luminosity is expected for ages older than 40 Myrs, when supernovae Type II cease. However, as noted earlier, the cooling times for the hot gas can be quite long, and hot gas can build up in the regions over an extended period, thus our instantaneous estimates of XPEs may not be very accurate for these regions.

We derived XPEs for the Antennae and NGC 2403 regions in the same way as we did the hinge clumps. For the Antennae regions with $\geq 3\sigma$ detections in the X-ray, we find XPEs ranging from 0.16% to 0.91%, with a median of 0.38%, after eliminating the regions with bright X-ray point sources. These values are similar to the XPEs found for the hinge clumps. For the NGC 2403 regions, we find a lower median XPE of 0.16%. In all cases, we find a large range in the derived XPEs, perhaps reflected the uncertainties in these estimates.

In Figures 11 though 14, we plot XPE against Hα equivalent width, Spitzer [3.6] − [24] color, N_H, and $n_e\sqrt{f}$. The XPE for the NGC 2207 clump is similiar to or higher than that of the other hinge clumps and regions within the Antennae, in spite of its low observed L_X/L_{24} ratio (see Figure 4). This suggests that its low observed L_X/L_{24} ratio is primarily caused by high absorption, rather than by extremely young age. It has the highest inferred N_H of the hinge clumps (see Table 12) thus the largest correction for extinction, but only a moderate Hα equivalent width.

Antennae region 3 has an XPE similar to that of NGC 2207-1 but a lower inferred column density and a higher Hα equivalent width. Thus it appears younger but less obscured. Antennae region 4 has a low inferred XPE and a high implied column density. Region 4 in the Antennae does not have an extremely high Hα equivalent width (Figure 11), in spite of the very young estimated age of 1 Myrs for the most luminous cluster WS80 in this region (Whitmore et al. 2010). This suggests that region 4 contains a wide range of stellar ages and extinctions. The extinction of the Hα line towards the youngest stars may be significantly higher than that of the observed red stellar continuum, which would artificially bias the observed Hα equivalent width towards older ages.

The three hinge clumps that are undetected by Chandra (Arp 270-2, Arp 270-3, and Arp 270-4) have XPE upper limits consistent with the X-ray detections of the other hinge clumps and the detected Antennae regions (Figures 11 − 13). This suggests that their lack of X-ray emission is simply due to low SFRs. They have the lowest SFRs in our sample (Table 10) with the exception of Arp 270-1, which has a candidate ULX. Arp 270 is the closest system in our sample, thus our selection criteria reaches lower luminosities for clumps in Arp 270 than for the other galaxies.

A weak correlation between XPE and Hα equivalent width is visible in Figure 11, while the XPEs do not correlated with the [3.6] − [24] colors of these clumps (Figure 12). Theoretical studies

suggest that the X-ray production efficiency in star forming regions should increase with time (Silich, Tenorio-Tagle, & Añorve-Zeferino 2005; Añorve-Zeferino, Tenorio-Tagle, & Silich 2009; Hopkins, Quataert, & Murray 2012). The large scatter in this plot may be because there is likely a range of stellar ages and/or extinctions within a clump, thus our simple estimate of XPE using a single age and single extinction is quite uncertain. In addition, there may be contributions from HMXBs to the extended X-ray emission in these regions, which are not taken into account in our calculation of the XPE. Another factor is the timescale for cooling of the hot gas; hot gas can build up in the region over an extended period, thus the rate of mechanical energy injection into the region from the star formation should be averaged over an extended time period.

We also see a weak correlation between XPE and hydrogen column density N_H (Figure 13), and between XPE and $n_e\sqrt{f}$ (Figure 14), when excluding the sources that are likely ULXs. This is consistent with theoretical expectations, which suggest that XPE should increase with increasing gas density (Silich et al. 2005; Anorve-Zeferino et al. 2009; Hopkins et al. 2012). Lower density gas allows stellar winds to escape more freely, while higher density gas would incur more collisions thus producing more X-ray emission. The large scatter in XPE with $n_e\sqrt{f}$ (Figure 14) may be due in part to the large uncertainties on both of these quantities. In addition to uncertainties in the derived stellar ages and the possibility that there is a range of ages within the clumps, other contributing factors may be uncertainties in the measured angular extent of the X-ray emission which is a function of sensitivity, as well as uncertainties in the line-of-sight path length through the ionized region.

9. Summary and Discussion

We have investigated the properties of a visually-selected sample of 12 bright hinge clumps in five interacting galaxy systems. We limited our sample to those with extensive multi-wavelength archival data available including GALEX UV, Spitzer IR, 2MASS, Hα, and SDSS imaging. Most critically, we have also examined high-resolution HST images of the hinge clumps to investigate their morphology in detail and Chandra X-ray data to study their hot gas and luminous X-ray binary populations. Comparisons have been made with star-forming regions in the Antennae galaxies and in the normal spiral NGC 2403. Some of these hinge clumps are forming stars at prodigous rates, between $1 - 9$ $M_\odot$ yr^{-1}, higher than the global values for many normal spiral galaxies, while others are more quiescent.

We find remarkably large ($\sim$70 pc) and luminous ($M_I \sim -12.2$ to -16.5) UV/optical sources at the centers of these clumps. These sources are sometimes embedded in long arcs or linear ridges containing fainter star clusters, suggestive of star formation along a narrow caustic. The sizes of these central sources are much larger than typical super star clusters, and their luminosities are near the high luminosity end of the super star cluster luminosity function. These results suggest that they are likely composed of close concentrations of multiple star clusters, rather than individual clusters.

Comparison to stellar population synthesis models suggests that the hinge clumps contain a range of stellar ages. This is consistent with expectations based on models of interacting galaxies which predict prolonged inflow of gas into the hinge region, producing sustained star formation or multiple bursts rather than a single instantaneous burst. The central sources seen in the HST images are bluer on average than the clump as a whole, again suggesting a range of stellar ages within the clump. A jewel-in-the-crown mode of star formation may operate within hinge clumps, in which luminous young star clusters form within a 'crown' of older stars, dispersed from earlier star formation episodes.

These results all indicate that hinge clumps, as a population, are relatively long-lived structures. How long hinge clumps persist and form stars is an unanswered question. Our selection criteria for this study selected targets that are bright in either UV or 24 μm light, which restricts our sample clumps to be younger than $\sim$100 Myr, the lifetime of the UV-producing stellar population. However, our morphological definition of hinge clumps, that they are discrete knots of recent star formation in the inner half of a tidal feature, can include fainter and presumably older structures.

Analytical and numerical models (Struck & Smith 2012) suggest hinge clumps arise in regions

of global compression formed by multiple converging density waves that produce ocular waves and caustics in the outer disks of interacting galaxies. These structures may be long lived but are more subject to shear in the relatively flat rotation curve environment of outer disks compared to nuclear starbursts that reside near the bottom of the galaxy potential. The models suggest much more intense interaction between azimuthal and radial caustic waves in the outer disk, near the base of the tails, than elsewhere in the system in the pre-merger stage of a tail-producing encounter.

Determining how long hinge clumps may last and their ultimate fate depends on the specific details of the galaxy interaction that produced them. While the dynamical explanation for hinge clump formation appears robust, current simulations lack sufficient resolution and the necessary microscale physics needed to make reliable predictions of their ultimate fate. However, if the galaxy interaction is a simple flyby, then it is likely that the larger hinge clumps will eventually spiral into the nucleus through dynamical friction while the smaller ones may disperse through shear in a few rotation periods. If the galaxy interaction results in a merger, the star clusters within hinge clumps may be dispersed intact as self-gravitating bodies and may eventually become globular clusters. It is uncertain if and how such globular clusters could be differentiated from the ordinary populations of old globular clusters.

Several of the hinge clumps studied in this work are prodigous X-ray emitters ($L_X \sim 10^{40} - 10^{41}$ erg s^{-1}). In most cases, this emission appears extended and is best interpreted as originating from a hot, $\sim$0.3 keV, thermal plasma. Hot gas is expected in regions of intense star formation. Where this gas is confined by dense surrounding cooler interstellar medium, the hot gas cooling times are short and the energy input into the hot gas is quickly radiated away giving rise to a high X-ray luminosity. In lower-density regions, in contrast, hot gas bubbles do $P\,dV$ work on the surroundings giving rise to galactic winds but with little radiative losses (Hopkins, Quataert, & Murray 2012). The converging flow of gas and stellar orbits that produce hinge clumps may be sufficient to confine the hot gas produced by supernovae and stellar winds and thus produce the high X-ray luminosities and high XPEs observed in several of our sample hinge clumps, similar to those of star forming regions within the merging Antennae galaxies. In contrast, the star forming regions in the normal spiral galaxy NGC 2403 have lower XPEs, consistent with their lower inferred electron number densities and hydrogen column densities.

In three of the hinge clumps, the X-ray emission is either point-like or point-like with an underlying extended soft component (Arp 240-4). In one case (Arp 240-3), the X-ray spectrum and luminosity indicate a compact star forming region; the other two sources are likely ULXs. Arp 240-4 is the most X-ray luminous hinge clump in the sample, with a hard X-ray spectrum and an extreme X-ray luminosity of $\sim 2 \times 10^{41}$ erg s^{-1}. This luminosity is difficult to explain by a single HMXB; it may be a collection of HMXBs or alternatively, an intermediate-mass black hole. If this source is indeed an intermediate-mass black hole, its mass is $1600 - 16{,}000$ $M_\odot$, assuming it is radiating at $10\% - 100\%$ of the Eddington luminosity. The ratio of the mass of this black hole to the stellar mass of this clump (Tables 11 and 12) would then be 1.5×10^{-4} to 7.3×10^{-6}. Massive clumps and clusters hosting intermediate mass black holes may eventually migrate into the center of the galaxy, where the black holes may merge into supermassive central black hole (e.g., Ebisuzaki et al. 2001; Elmegreen et al. 2008).

This research was supported by NASA Astrophysics Data Analysis Grant ADAP10-0005 and National Science Foundation Extragalactic Astronomy grant AST-1311935. We thank the anonymous referee for helpful suggestions. We also thank Michele Kaufman, Debra Elmegreen, Hongxin Zhang, Yu Gao, Howard Bushouse, Javier Zaragoza-Cardiel, Marcel Clemens, and Liese van Zee for providing copies of their data and helpful communications. We thank Mark Hancock for the use of his scripts to determine population ages. This research has made use of the NASA/IPAC Extragalatic Database (NED), which is operated by the Jet Propulsion Laboratory, California Institute of Technology, under contract with NASA. This work is based in part on observations made with the Spitzer Space Telescope, which is operated by the Jet Propulsion Laboratory (JPL), California Institute of Technology under a contract with NASA. This re-

search is also based in part on observations made with the NASA/ESA Hubble Space Telescope, and obtained from the Hubble Legacy Archive, which is a collaboration between the Space Telescope Science Institute (STSci/NASA), the Space Telescope European Coordinating Facility (ST-ECF/ESA) and the Canadian Astronomy Data Centre (CADC/NRC/CSA). This study also uses data from the NASA Galaxy Evolution Explorer (GALEX), which was operated for NASA by the California Institute of Technology under NASA contract NAS5-98034. This research has also made use of data obtained from the Chandra Data Archive and software provided by the Chandra X-ray Center (CXC). This publication makes use of data products from the Two Micron All Sky Survey, which is a joint project of the University of Massachusetts and the Infrared Processing and Analysis Center/California Institute of Technology, funded by the National Aeronautics and Space Administration and the National Science Foundation. This research has made use of the NASA/IPAC Infrared Science Archive, which is operated by JPL, the California Institute of Technology, under contract with the National Aeronautics and Space Administration.

Appendix I: Morphologies of Individual Galaxies

A. Arp 82 (NGC 2535/6)

Arp 82 is an unequal mass pair with a long tail extending to the north (Figure 15 left). The more massive galaxy in the north NGC 2535 has an ocular structure (Elmegreen et al. 1991; Kaufman et al. 1997; Hancock et al. 2007). In an earlier study (Hancock et al. 2007), we conducted a detailed analysis of the GALEX/Spitzer/Hα photometry of numerous clumps of star formation in Arp 82. Luminous knots of star formation are present along the eyelids and points of the ocular (Hancock et al. 2007). In the current study, we target the most luminous knot of star formation in the tidal features, which lies near the base of the northern tail (marked in Figure 15). We classify this region as a hinge clump. This knot shows up as a discrete source in the 20 cm radio continuum image and the 21 cm HI map of Kaufman et al. (1997).

In Figure 16, we present a close-up view of the HST F606W image of the hinge clump. In the center of this clump, we find a very luminous source with absolute I magnitude $M_I \sim -13.3$. This source is unresolved with HST (diameter $\leq$ 70 pc). This object lies near the center of a straight line of lower luminosity star clusters that extends 15″ (4 kpc) in length. This linear structure suggests star formation along a caustic, perhaps caused by local gravitational instability and competitive cluster growth in a linear pile-up zone.

Arp 82 has not been observed with Chandra.

We presented a numerical simulation of the Arp 82 interaction in Hancock et al. (2007). The model indicates that the long tail was produced in a prograde planar encounter, with the companion in an elliptical orbit around the primary. In the right panel of Figure 17, we display an analytical model of a prolonged prograde interaction (approximated by three tidal impulses) from Struck & Smith (2012) (Figure 12 in that paper). We compare with a close-up view of the Arp (1966) Atlas photograph of the hinge region of Arp 82 (left panel). Note the resemblance between the model and the galaxy. The inner disk of the model galaxy shows an ocular structure similar to that in NGC 2535. A larger oval-shaped structure is visible in the model outside of the inner ocular. This structure is produced when two caustics diverge and one arcs back to the main galaxy. Arp 82 shows a similiar morphology in the northeast, where a spiral arm loops back towards the main galaxy. Further along the model tail to the north, two caustics converge, causing a narrowing of the tail. In the Arp picture, a similar narrowing of the tail occurs at the location of the hinge clump, and a faint arc is visible extending to the west. This suggests that the star formation in the hinge region was triggered by intersecting caustics.

B. Arp 240 (NGC 5257/8)

Figure 18 compares the HST F435W image of Arp 240 with the Spitzer 8 μm image. Arp 240 is a pair of disk galaxies with similar masses, with a connecting bridge and two short tails extending from the two galaxies. Both galaxies in the pair are independently classified as 'Luminous Infrared Galaxies' (LIRGs), with far-infrared luminosities of 2×10^{11} $L_\odot$ (Howell et al. 2010). Arp 240 has a total of five clumps that we define as hinge clumps, one in the southeastern galaxy of the pair (NGC 5258), and four in the northwestern galaxy (NGC 5257). These are marked in Figure 18. X-ray emission is detected from all five of these clumps.

Arp 240W has an inner spiral, along with two clumpy ridges of star formation to the west and east of this spiral, at the base of the tails. In the Spitzer 8 μm image of Arp 240W, three knots of star formation are seen along the base of the southern tail, and a fourth at the base of the northern tail. These four regions are all bright in the CO (3−2) map of Wilson et al. (2008) as well as in the Bushouse (1987) Hα map.

A closer view by HST of Arp 240W (Figure 19 left) shows that each of the four hinge clumps in this galaxy contains a central luminous source. The absolute B magnitudes M_B of these sources range from −14.4 for Arp 240-4 to −15.1 for Arp 240-1, while M_I ranges from −14.4 for Arp 240-4 to −15.6 for Arp 240-2. These clusters are resolved in the HST images, with FWHM between ∼40 pc for Arp 240-2 to ∼100 pc for Arp

240-3. In the HST images, the brightest optical source in clump 2 is about 2″ off from the 8 μm peak, but well within the 5″ radius used for the Spitzer photometry. For clump 3, the brightest optical source is about 1″ from the 8 μm peak. For clump 1, the source that is the brightest in the HST UV and optical images is not the brightest in the near-infrared F160W image. Both of these sources are about 3″ from the 8 μm peak.

In Figure 19 (right), we overlay a smoothed version of the Chandra 0.3 − 8 keV map on the HST F814W image of Arp 240W. Diffuse X-ray emission is present along the base of the tidal features; this extended emission is predominantly soft X-rays. Clump 4, at the base of the northern tail, has a bright compact source with a hard X-ray spectrum. Clump 3 is also compact in the X-ray, however, its spectrum is intrinsically soft (see Section 3.3).

In Figure 20, we compare the HST F814W image of Arp 240W with an analytical model from Struck & Smith (2012) (Figure 10 from that paper, inclined to match the observed inclination of Arp 240W). In the model, two embedded oculars are seen. In Arp 240W, the inner spiral is not completely closed into an ocular, unlike in the model. In a ridge along the base of the southern tail lies three regions we classify as hinge clumps (see Figure 19). The extreme star formation in this region may be due to overlapping caustics, as in the model. A similar overlap of caustics may be responsible for clump 4 near the base of the northern tail.

Arp 240E has a bright mid-infrared source at the base of the southern tail (Figure 18). This region is the brightest CO (3−2) source in the galaxy (Wilson et al. 2008). In the HST images (Figure 21), this clump has an extremely luminous optical source near its center, with $M_B \sim -15.8$ and $M_I \sim -16.5$. This source is unresolved in the HST images (FWHM $\leq$ 75 pc). It lies along a distorted arm-like structure, and is flanked by two fainter sources ∼170 pc (0.″35) away along the arm. The X-ray map shows strong extended X-ray emission from this region (Figure 21 right). Because of the high inclination of this galaxy and its very distorted structure, unlike Arp 240W we are not able to match it to one of our analytical models. However, the location and luminosity of the star formation region suggests it may be a hinge clump.

C. Arp 256

Arp 256 is a widely separated pair of spirals (Figure 22). The southern galaxy has a far-infrared luminosity of 2.8×10^{11} $L_\odot$, thus it is classified as a LIRG, while the northern galaxy has $L_{FIR} = 2.3 \times 10^{10}$ $L_\odot$ (Howell et al. 2010). According to an archival 70 μm Herschel image, most of the far-infrared luminosity from the southern galaxy comes from the inner disk, while the far-infrared light from the northern galaxy is dominated by a luminous knot of star formation at the base of its long northern tail. We classify this knot as a hinge clump.

In Figure 22, we compare the HST F435W image of Arp 256 with the Spitzer 8 μm image. In addition to the hinge clump in the northern tail, the northern galaxy in Arp 256 has a tidal dwarf galaxy near the end of its southern tail. A 21 cm HI map of this system has been presented by Chen et al. (2002), which shows that these tails are gas-rich. The hinge clump is very bright in the 20 cm radio continuum (Chen et al. 2002).

In Figure 23, we display a close-up view of the HST F814W image of the hinge clump. This region is resolved in the HST red and near-infrared images into a flattened structure with a FWHM ∼ 70 pc, much larger than the typical size of the super-star clusters found in interacting galaxies (∼3 pc; Larsen 2004). This source is extremely luminous ($M_B \sim -14.6$ and $M_I \sim -14.8$). In the HST UV image, this source resolves into two peaks separated by ∼0.″15 (80 pc) north/south; this double structure may be due to dust absorption; alternatively, the slightly higher spatial resolution in the UV may be resolving a pair of clusters. As in Arp 82 and 240, this source is embedded in a linear ridge of star clusters. This ridge lies along the leading edge of the tidal tail. The X-ray emission from this region (Figure 21, right panel) is extended, with two possible peaks.

As with Arp 82, the long northern tail of Arp 256N signals a prograde planar encounter. In an earlier study, we produced a numerical simulation of the similar system Arp 305 (Hancock et al. 2009). This same

simulation can be applied to Arp 256, but at an earlier timestep (see the second panel in Figure 4 in Hancock et al. 2009). A closer look at the northern tail of Arp 256N shows a double structure (Figure 24). We find an approximate match to this tidal morphology using the same analytical model as for Arp 82, but at an earlier timestep. This is illustrated in Figure 25, where we compare the HST images of Arp 256N with this analytical model (3rd panel from Figure 12 in Struck & Smith 2012). Note the two approximately parallel caustics along the model tail. In the Arp 256 tail, the hinge clump lies near where the two main filaments in the tail intersect (see Figure 25).

In the HST images (Figure 25), two UV-bright knots of star formation are visible out of the main disk of the galaxy, above and below the bulge of the galaxies. The numerical model suggests that that star formation was triggered by material pulled out from the galaxy by the interaction, which is now falling back in on the disk. These star forming regions produce the characteristic 'X' shape seen in the inner region of Arp 256 in the Arp (1966) Atlas photograph (Figure 24).

D. Arp 270 (NGC 3395/6)

The GALEX NUV and Spitzer 8 μm images of Arp 270 are displayed in Figure 26. Arp 270 is a close pair of equal-mass spiral galaxies with a $10'$ (79 kpc) long HI tail stretching from the eastern edge of the pair and extending to the south and west (Clemens et al. 1999). We include four tidal star forming regions in Arp 270 in our hinge clump sample. All four of these are associated with the western galaxy NGC 3395. The first three Arp 270 clumps have the lowest Hα luminosities ($<10^{40}$ erg/s) of the hinge clumps in our sample (see Table 6). Only one of the four hinge clumps in Arp 270 was detected in the X-ray, clump 1 (Figure 27 right). This source was included in our earlier survey of X-ray point sources in Arp galaxies (Smith et al. 2012). As noted in Section 3.3, this source has a soft X-ray spectrum. This source is coincident with the Spitzer mid-infrared position, which is a bit offset from the UV peak. A number of other X-ray point sources are detected in Arp 270, but none of these are associated with the other hinge clumps. Diffuse X-ray emission is seen in the inner region of the galaxy, but not in the hinge clumps.

Based on a numerical simulation, Clemens et al. (1999) conclude that the Arp 270 encounter is prograde with respect to the western galaxy NGC 3395 and retrograde with respect to the edge-on galaxy in the east NGC 3396, and the two galaxies are on their second approach. They conclude that the long HI tail originated from the western galaxy NGC 3395, and its apparent connection to NGC 3396 is a projection effect. In this model, the tail originates from the western side of NGC 3395 and arcs around behind NGC 3396 (Clemens 1998). In optical images (Figure 27), NGC 3395 has two tail-like structures extending to the west: the outer tail containing our target clumps, and an inner spiral. Whether the long HI tail connects to the outer tail or the inner spiral is uncertain.

None of the analytical models in Struck & Smith (2012) resemble NGC 3395 in any detail, perhaps because of its warped and distorted structure. The closeness of the two galaxies in this pair argues that this system is in a later stage of evolution than the other systems in our sample and closer to merger, thus it is harder to model analytically. We include the four marked regions in our sample as possible hinge clumps due to their apparent location near the base of tidal features and the availability of high sensitivity Chandra data, however, whether or not their formation was triggered by intersecting caustics is uncertain. The only HST images of Arp 270 do not cover the hinge clumps (Hancock et al. 2003), thus we do not have high resolution optical images available to study the morphology of these regions in more detail.

E. NGC 2207

IC 2163 and NGC 2207 are two spiral galaxies with similar masses in a very close interacting pair. In Figure 28, we display the GALEX NUV and Spitzer 8 μm images of this pair. The Spitzer images of this system were previously presented by Elmegreen et al. (2006), who noted an extremely mid-infrared-bright knot of star formation on the western edge of NGC 2207. This source, which they call 'feature i', is our hinge

clump candidate, and lies in a distorted spiral arm at the base of a short tail-like feature visible in optical images. Feature i lies near a massive concentration of HI gas ($\sim 10^9$ $M_\odot$); a second similar concentration (8×10^8 $M_\odot$) is seen $1'$ (11 kpc) to the north of knot i (Elmegreen et al. 1995). This second HI cloud does not have an optical or infrared counterpart, and may be a gas-rich extension of the tail-like feature containing feature i. The companion galaxy IC 2163 to the east has an ocular structure (Elmegreen et al. 1991, 2006), with an HI tail extending to the east (Elmegreen et al. 1995). Strong star formation is seen in the 'eyelids' and 'points' of this ocular (Elmegreen et al. 1995, 2006).

The Spitzer mid-infrared peak for feature i is offset slightly from the GALEX NUV peak, likely because of obscuration. Feature i is the brightest radio continuum source in the galaxy (Vila et al. 1990; Kaufman et al. 2012). The 6 cm/20 cm spectral index is consistent with non-thermal emission in the radio (Vila et al. 1990). Kaufman et al. (2012) noticed a possible increase in 6 cm flux between 1986 and 2001, and suggested a possible radio supernova.

The HST images of NGC 2207 were previously analyzed by Elmegreen et al. (2001), before the Spitzer images were obtained. In that study, they only considered the optically brightest clusters, which did not include the cluster in the center of the mid-infrared object feature i. The HST morphology of the NGC 2207 hinge clump (Figure 29) differs somewhat from that of the other hinge clumps in our sample. The dominant source in the NGC 2207 hinge clump is at the center of a more extended grouping of fainter clusters, rather than in a straight line of clusters. However, this group of clusters is part of an extended ridge of star formation along a spiral arm/short tail-like structure, thus it may also have been produced by star formation along a caustic, albeit a more distorted caustic.

The source at the center of this clump is extended in the HST images, with FWHM $\sim$ 70 pc. Its observed absolute I magnitude is only about -12.2, however, its intrinsic luminosity might be much higher if it is strongly obscured. As noted by Kaufman et al. (2012), there is a dust lane visible in optical images that runs across feature i. The extinction to this clump is discussed further in Section 7.3.

The unsmoothed X-ray map of the NGC 2207 hinge clump is shown in Figure 29 (right). This source is quite extended with Chandra but with a low surface brightness, and has a soft X-ray spectrum. The Chandra data for this source was previously analyzed by Mineo et al. (2013), who also concluded that the source is soft and extended with Chandra, and found an observed flux similar to ours.

We classify feature i as a possible hinge clump based on its location near the base of a short tail-like structure and its strong mid-infrared emission. However, this classification is uncertain because of the shortness of the tail and the peculiar morphology, which differs from that of the other systems in our sample. Feature i may instead be a tidally-disturbed disk region rather than a true tidal structure.

The NGC 2207/IC 2163 encounter has been modeled numerically by Struck et al. (2005), who conclude that the collision was prograde with respect to IC 2163, and retrograde for NGC 2207. In contrast, the other hinge clumps in our sample all lie in longer tidal features produced by prograde encounters. However, the basic mechanism of star formation triggering due to intersecting caustics may still hold for feature i. Models suggest that the eastern HI tail of IC 2163 may eventually develop hinge clumps, once sufficient time has elapsed for strong waves to develop and intersect in that region.

Appendix II: Comparison to the Antennae

A. Overview

To put our hinge clumps in perspective, we compare them to the well-studied 'overlap' region of intense star formation between the two disks of the Antennae galaxies. Like the hinge clumps, this region is not in a galactic nucleus, thus it is easier to study and less confused than nuclear starbursts. At a distance of only 24.1 Mpc, the Antennae provides much better spatial resolution than the hinge clump galaxies, thus it provides a good comparison system. The star clusters in the Antennae have been investigated in a number

of studies, including a detailed population synthesis study by Whitmore et al. (2010).

In Figure 30, we provide a multi-wavelength mosaic of the Antennae overlap region, including the co-added Chandra $0.3 - 0.8$ keV map (upper left panel), an archival HST ACS F814W (I band) image from the Hubble Legacy Archive (upper right panel), an archival HST WFC3 F160W image (near-infrared H band) (middle left panel), and the Spitzer 8 μm map (middle right panel). We also compare to a 230 GHz millimeter continuum map and a CO(2−1) map, respectively, from the Atacama Large Millimeter/submillimeter Array (ALMA) telescope, previously presented by Espada et al. (2012) and obtained from the ALMA science portal[7] (lower left and low right panels in Figure 30). On these images we superimpose circles marking two of the $4\farcs5$ radius regions studied by Zhang, Gao, & Kong (2010): their region 3 (right) and region 4 (left). Region 4 lies near the peak of the 8 μm and 24 μm emission, and has been called the mid-infrared 'hot spot'. It has the reddest [3.6] − [24] color of all the Antennae regions studied by Zhang, Gao, & Kong (2010) (see Section 5). Region 3 is also quite bright in the mid-infrared, and is the second reddest region in [3.6] − [24] in their survey. These red colors imply intense and obscured star formation in these regions.

B. Region 4

From the $L_{24}/L_{H\alpha}$ ratio we determine an extinction of $A_V = 3.23$ towards region 4. Probably because we are averaging over the entire region, this value is significantly less than that found by Whitmore et al. (2010) towards the brightest cluster visible in Region 4 in the HST F814W image, for which they estimate $E(B - V) = 2.44$. This cluster is also extremely massive, 8.2×10^6 $M_\odot$, and has an extinction-corrected $M_V = -15.4$ (Whitmore et al. 2010). This object is sometimes called 'WS80', being object number 80 in the Whitmore & Schweizer (1995) study. Whitmore et al. (2010) derive an age of only 1 Myrs for this cluster. Whitmore & Zhang (2002) associate WS80 with the brightest 6 cm radio continuum source in the Antennae, as seen in the Neff & Ulvestad (2000) maps. The radio spectrum of this source indicates that this emission is predominantly thermal. The WS80 cluster is associated with the brightest CO(1-0) emission in the Antennae (Wilson et al. 2000). As seen in the ALMA maps in Figure 30, this source is also very bright in CO(2-1) and in the 230 GHz continuum.

In the HST images, WS80 is surrounded by fainter emission, probably from nearby lower luminosity clusters, but no other clusters with similar luminosities. In subarcsecond resolution mid-infrared images, Snijders et al. (2006) detect a possible second mid-infrared source $0\farcs54$ to the northeast of WS80, which is not seen in optical or near-infrared images. They suggest that this may be a highly obscured cluster with $A_V \geq 72$, which implies $N_H \geq 10^{23}$ cm^{-2}. In very high resolution 3.6 cm radio continuum maps, a second fainter source is seen at this location, along with an H_2O radio maser (Brogan, Johnson, & Darling 2010).

As seen in Figure 30, Region 4 in the Antennae is considerably fainter in the X-rays than Region 3. Region 4 hosts a moderately bright X-ray point source which lies $\sim 0\farcs5$ southwest of WS80. This point source is embedded in extended X-ray emission that extends to the north towards WS80. From the archival Chandra data, we extracted the X-ray spectrum for both region 4 as a whole (using a $4\farcs5$ radius aperture), and for the point source (with a $1\farcs4$ radius aperture). Region 4 as a whole shows a composite X-ray spectrum, with both a power law and a thermal component with $kT = 0.68 \pm 0.13$ keV. More than half of the power law flux arises from the point source. The point source has a pure power-law spectrum with $L_X \sim 3 \times 10^{38}$ erg/s.

If the Whitmore et al. (2010) age estimate for WS80 of 1 Myrs is accurate, WS80 itself is too young to host HMXBs or to have developed supernovae. The point source may be a HMXB associated with a nearby slightly older stellar population, while the diffuse X-ray emission in this region may be powered by supernovae associated with an earlier generation of stars or hot star winds rather than supernovae. The spatial offset between the X-ray, the optical, and the mid-infrared sources in Region 4 suggest an age sequence from older in the southwest to younger in the northeast.

[7] http://almascience.nao.ac.jp/almadata/sciver/AntennaeBand6

C. Region 3

In contrast to WS80 in region 4, the brightest cluster in Zhang, Gao, & Kong (2010) region 3 is closely surrounded by other bright clusters. This complex of clusters is known as 'Knot B' (Rubin et al. 1970; Whitmore et al. 2010). Whitmore et al. (2010) find a range of ages for the clusters in this complex from 2.5 Myr to 50 Myr, with the youngest ages found preferentially to the east. They suggest that this may be a case of sequential triggered star formation. The clusters in Knot B are significantly less obscured than WS80 in Region 4 but still quite reddened, with $E(B-V) \sim 0.12 - 1.0$ (Whitmore et al. 2010). The most massive cluster in Knot B is almost as massive as WS80, with 5.0×10^6 $M_\odot$. This region is much fainter in CO than WS80.

Most of the diffuse X-ray emission from Region 3 is located near Knot B. In addition, an X-ray point source lies approximately $3''$ to the south of knot B near an optical point source. The extracted X-ray spectrum of this source appears very absorbed, implying a very large intrinsic L_X. Its spectrum has a peak near 3 keV, and can be fit with a disk blackbody model with $kT \sim 0.75 - 1$ keV.

D. Comparison to Our Hinge Clumps

The large apparent sizes and the high luminosities of the objects seen in the centers of the hinge clumps by HST may be caused by the blending of multiple clusters very close together. We can make use of the relative proximity of the Antennae star forming regions to explore some of the results of this blending. We investigate what Regions 3 and 4 would look like in HST images if they were at the distance of our hinge clumps. We smoothed the HST F814W image with a Gaussian to the effective resolution it would have if it were at a distance of 102 Mpc (the distance of Arp 240). The clusters in Knot B of Region 3 become blended together into a single extended object with FWHM $\sim$ 110 pc $\times$ 120 pc. In Region 4, the WS80 region is only marginally resolved in the smoothed image, with FWHM $\sim$ 80 pc. This exercise suggests that the extended sources we are seeing in the HST images of the hinge clumps could be blended complexes of clusters that are very closely packed together.

We note that larger than normal clusters have also been found in the tidal features of the merger remnant NGC 3256 and Stephan's Quintet by Trancho et al. (2007, 2012). These authors suggest that the large sizes may be a consequence of less tidal stripping of the outer stars in these clusters or weak compression at the time of formation. It is possible, however, that the NGC 3256 and Stephan's Quintet sources are also multiple clusters blended together, however, at 37 Mpc and 88 Mpc, respectively, they are not as distant as some of the hinge clumps in our sample.

At the distance of Arp 82 (53 Mpc), Antennae regions 3 and 4 would be included in a single $5''$ Spitzer and GALEX aperture. The [3.6] $-$ [24] color would still be quite red, although these regions contain a range of stellar ages. An area on the Antennae equivalent to that covered by our $5''$ aperture at Arp 82 would be observed to have a [3.6] $-$ [24] color of 8.7, similar to the value for region 3 alone. If the Antennae were further away, at the distance of Arp 240, the southern nucleus would be included in a $5''$ beam along with regions 3 and 4. Thus the Antennae overlap region is not a perfect analogy to the hinge clumps, as it is closer to its nucleus than the hinge clumps are to their galactic nuclei.

In the Chandra map of the Antennae shown in Figure 30, outside of region 3 to the southeast is a ridge of diffuse X-ray emission. This ridge continues several arcseconds to the southeast beyond the field of view of the figure. This ridge of emission was studied by Metz et al. (2004), who concluded that it was likely caused by faint older stars ($\sim$100 Myrs). In the HST F814W and F160W images, a few faint star clusters are seen along this ridge. If the Antennae were at the distance of Arp 240, this ridge of emission would be included in our $5''$ apertures. The X-ray luminosity of this ridge is larger than that of knot B itself, thus its inclusion in the beam would more than double the observed X-ray flux.

This comparison to the Antennae emphasizes that care must be taken in our interpretation of the constituents of hinge clumps, especially those at greater distances. Within our hinge clumps there is likely

a range of stellar ages and extinctions, making detailed population synthesis difficult. As with Antennae regions 3 and 4, the X-ray emission from the hinge clumps may be due to a combination of diffuse gas and HMXBs, again making interpretation difficult. These points underline the cautions we give in Sections 7 and 8, where we compare colors and fluxes of the hinge clumps to simple population synthesis models.

We note that linear structures made of star clusters are also seen in the Antennae. Whitmore et al. (2010) suggest that these structures were produced by either sequential triggered star formation or large-scale processes such as a density wave or a collision between two large clouds.

REFERENCES

Anders, P. & Fritze-v. Alvensleben, U. 2003, A&A, 401, 1063.

Añorve-Zeferino, G. A., Tenorio-Tagle, G., & Silich, S. 2009, MNRAS, 394, 1284

Antoniou, V., Zezas, A., Hatzidimitriou, D, & Kalogera, V. 2010, ApJ, 716, L140

Arp, H. 1966, Atlas of Peculiar Galaxies (Pasadena: Caltech)

Bastian, N., Gieles, N., Efremov, N., & Lamers, H. J. G. L. M. 2005, A&A, 443, 79

Belczynski, K., Bulik, T., Fryer, C. L., Ruiter, A., Valsecchi, F., Vink, J. S., & Hurley, J. R. 2010, ApJ, 714, 1217

Berg, D. A., Skillman, E. D., Garnett, D. R., Croxall, K. V., Marble, A. R., Smith, J. D., Gordon, K., & Kennicutt, R. C., Jr. 2013, ApJ, in press

Bell, E. F. & de Jong, R. 2001, ApJ, 550, 212

Bell, E. F., McIntosh, D. H., Katz, N., & Weinberg, M. D. 2003, ApJS, 149, 289

Beirão, P., Appleton, P. N., Brandl, B. R., Seibert, M., Jarrett, T., & Houck, J. R. 2009, ApJ, 693, 1650

Bogdán, A. & Gilfanov, M. 2011, MNRAS, 418, 1901

Bohlin, R. C., Savage, B. D., & Drake, J. F. 1978, ApJ, 224, 132

Böker, T., Sarzi, M., McLaughlin, D. E., van der Marel, R. P., Rox, H. W., Ho, L. C., & Shields, J. C. 2004, AJ, 127, 105

Boquien, M., Duc, P.-A., Braine, J., Brinks, E., Lisenfeld, U., & Charmandaris, V. 2007, A&A, 467, 93

Boquien, M., Duc, P.-A., Galliano, F., Braine, J., Lisenfeld, U., Charmandaris, V., & Appleton, P. N. 2010, AJ, 140, 2124

Boquien, M., Calzetti, D., Kennicutt, R., et al. 2009a, ApJ, 706, 553

Boquien, M., Duc, P.-A., Wu, Y., Charmandaris, V., Lisenfeld, U., Braine, J., Brinks, E., Iglesias-Páramo, J., & Xu, C. K. 2009b, AJ, 137, 4561

Boquien, M., Lisenfeld, U., Duc, P.-A., Braine, P., Bournaud, F., Brinks, E., & Charmandaris, V. 2011, A&A, 533, A19

Bournaud, F. & Duc, P.-A. 2006, A&A, 456, 481

Bournaud, F., Duc, P.-A., & Emsellem, E. 2008, MNRAS, 389, L8

Brassington, N., J., Ponman, T. J., & Read, A. M. 2007, MNRAS, 377, 1439

Brogan, C., Johnson, K., & Darling, J. 2010, ApJ, 716, L5 & Appleton, P. N. 2010, AJ, 140, 2124

Bruzual, G. & Charlot, S. 2003, MNRAS, 344, 1000

Bushouse, H. A. 1987, ApJ, 320, 49

Bushouse, H. A., Lamb, S. A., & Werner, M. W. 1988, ApJ, 335, 74

Cao, C. & Wu, H. 2007, AJ, 133, 1710

Calzetti, D., Armus, L., Bohlin, R. C., Kinney, A. L., Koornneef, J., & Storchi-Bergmann, T. 2000, ApJ, 533, 682

Calzetti, D. 2001, PASP, 113, 1449

Calzetti, D., Kinney, A. L., & Storchi-Bergmann, T. 1994, ApJ, 429, 582

Calzetti, D., et al. 2005, ApJ, 633, 871

Calzetti, D., Kennicutt, R. C., Engelbracht, C. W., et al. 2007, ApJ, 666, 870

Cardelli, J. A., Clayton, G. L., & Mathis, J. S. 1989, ApJ, 345, 245

Cedres, B., Cepa, J, & Tomita, A. 2005, ApJ, 634, 1043 Charmandaris, V.,

Clemens, M. S., 1998, Ph.D. Dissertation, Cambridge University.

Clemens, M. S., Baxter, K. M., Alexander, P., & Green, D. A. 1999, MNRAS, 308, 364

Chandar, R., & Rothberg, B. 2010, in Proceedings of the 'Galaxy Wars: Stellar Populations and Star Formation in Interacting Galaxies' Conference, ASP Conf. Proc. 423, 116

Chen, J., Lo, K. Y., Gruendl, R. A., Miao-Ling, P., & Gao, Y. 2002, AJ, 123, 720

Cowie, L., et al. 1995, AJ, 110, 1576

Cutri, R. M., Skrutskie, M. F., Van Dyk, S., et al. 2006, Explanatory Supplement to the 2MASS All Sky Data Release and Extended Mission Products

Dieball, A., Knigge, C., Zurek, D. R., Shara, M. M., Long, K. S., Charles, P. A., & Hannikainen, D. 2007, ApJ, 670, 379

Donner, K. J., Engstrom, S., & Sundelius, B. 1991, A&A, 252, 571

Draine, B. T., et al. 2007, ApJ, 663, 866

Duc, P.-A., Bournaud, F., & Masset, F. 2004, A&A, 427, 803

Ebisuzaki, T., Makino, J., Tsuru, T. G., et al. 2001, ApJ, 562, 19

Elmegreen, B. G., Bournaud, F., & Elmegreen, D. M. 2008, ApJ, 684, 829

Elmegreen, D. M. & Elmegreen, B. G. 2014, ApJ, in press

Elmegreen, D. M., Kaufman, M., Brinks, E., Elmegreen, B. G., & Sundin, M. 1995, ApJ, 453, 100

Elmegreen, B. G., Kaufman, M., & Thomasson, M. 1993, ApJ, 412, 90

Elmegreen, D. M., Elmegreen, B. G., Kaufman, M., Sheth, K., Struck, C., Thomasson, M., & Brinks, E. 2006, ApJ, 642, 158

Elmegreen, D. M., et al. 2001, AJ, 121, 182

Elmegreen, D. M., et al. 2009, ApJ, 701, 306

Elmegreen, D. M., Sundin, M., Sundelius, B., & Elmegreen, B. 1991, A&A, 244, 52

Engelbracht, C. W., Gordon, K. D., Rieke, G. H., Werner, M. W., Dale, D. A., & Latter, W. B. 2005, ApJ, 628, 29

Espada, D., Komugi, S., Muller, E., et al. 2012, ApJ, 760, L25

Fabbiano, G., Zezas, A., & Murray, S. S. 2001, ApJ, 554, 1035

Fabbiano, G., et al. 2004, ApJ, 605, L21

Farrell, S. A., Webb, N. A., Barret, D., Godet, O., & Rodrigues, J. M. 2009, Nature, 460, 73

Fazio, G. G., et al. 2004, ApJS, 154, 10

Förster Schreiber, N. M., et al. 2011, ApJ, 739, 45

Gallazzi, A. & Bell, E. F. 2009, ApJS, 185, 253

Garnett, D. R., Shields, G. A., Skillman, E. D., Sagan, S. P., & Dufour, R. J. 1997, ApJ, 489, 63

Gerber, R. A. & Lamb, S. A. 1994, ApJ, 431, 604

Gieles, M. 2010, in Proceedings of the 'Galaxy Wars: Stellar Populations and Star Formation in Interacting Galaxies' Conference, ASP Conf. Proc. 423, 123

Grimm, H.-J., Gilfanov, M., & Sunyaev, R. 2003, MNRAS, 339, 793

Gilfanov, M., Grimm, H.-J., & Sunyaev, R. 2003, MNRAS, 339, 793

Haan, S., et al. 2011, AJ, 141, 100

Hancock, M., Weistrop, D., Eggers, D., & Nelson, C. H. 2003, AJ, 125, 1696

Hancock, M., Smith, B. J., Struck, C., Giroux, M. L., & Hurlock, S. 2009, AJ, 137, 4643

Hancock, M., Smith, B. J., Struck, C., Giroux, M. L., Appleton, P. N., Charmandaris, V., & Reach, W. T. 2007, AJ, 133, 676

Hao, C.-N., Kennicutt, R. C., Johnson, B. D., Calzetti, D., Dale, D. A., & Moustakas, J. 2011, ApJ, 741, 12

Helou, G., et al. 2004, ApJS, 154, 253

Helou, G., Khan, I. R., Malek, L., & Boehmer, L. 1988, ApJS, 68, 151

Holtzman, J. A., Hester, J. J., Casertano, S., et al. 1995, PASP, 107, 156

Hopkins, P. F., Quataert, E, & Murray, N. 2012, MNRAS, 421, 3522

Howell, J. H., Armus, L., Mazzarella, J. M. et al. 2010, ApJ, 715, 572

Into, T. & Portinari, L. 2013, MNRAS, in press (astro-ph/1301.2178)

Kaufman, M., Brinks, E., Elmegreen, D. M., Thomasson, M., Elmegreen, B. G., Struck, C., & Klaric, M. 1997, AJ, 114, 2323

Kaufman, M., Grupe, D., Elmegreen, B. G., Elmegreen, D. M., Struck, C., & Brinks, E. 2012, AJ, 144, 156

Kennicutt, R. C., Jr. 1984, ApJ, 287, 116

Kennicutt, R. C., Jr., Keel, W. C., van der Hulst, J. M., Hummel, E., & Roettinger, K. A. 1987, AJ, 93, 1011

Kennicutt, R. C., Jr., Calzetti, D., Walter, F., et al. 2007, ApJ, 671, 333

Kennicutt, R. C., Jr., Hao, C.-N., Calzetti, D., et al. 2009, ApJ, 703, 1672

Kennicutt, R. C., Jr. & Evans, N. J. 2012, ARAA, 50, 531

Lapham, R. C., Smith, B. J., & Struck, C. 2013, AJ, 145, 130

Larsen, S. S. 2000, MNRAS, 319, 893

Larsen, S. S. 2004, A&A, 416, 537

Lawton, B., Gordon, K. D., Babler, B., et al. 2010, ApJ, 716, 453

Lebouteiller, V., Bernard-Salas, J., Whelan, D. G., Brandl, B., Galliano, F., Charmandaris, V., Madden, S., & Kunth, D. 2011, ApJ, 728, 45

Li, A. & Draine, B. T. 2001, ApJ, 554, 778

Li, J. T. & Wang, Q. D. 2013, astro-ph/1308.1933

Liu, J.-F., Bregman, J. N., & Irwin, J. 2006, ApJ, 642, 171

Leitherer, C., et al. 1999, ApJS, 123, 3

Matthews, L. D., et al. 1999, AJ, 118, 208

McCray, R. 1987, in Spectroscopy of Astrophysical Plasmas, ed. A. Dalgarno & D. Layzer (Cambridge: Cambridge Univ. Press), 260

McKee, C. F. & Cowie, L. L. 1977, ApJ, 215, 213

Metz, J. M., Cooper, R. L., Guerrero, M. A., Chu, Y.-H., Chen, C.-H. R., & Gruendl, R. A. 2004, ApJ, 605, 725

Mineo, S., Gilfanov, M., & Sunyaev, R. 2012a, MNRAS, 419, 2095

Mineo, S., Gilfanov, M., & Sunyaev, R. 2012b, MNRAS, 426, 1870

Mineo, S., Rappaport, S., Steinhorn, B., Levine, A., & Gilfanov, M. 2013, ApJ, 771, 133

Morrison, R. & McCammon, D. 1983, ApJ, 270, 119

Moustakas, J., Kennicutt, R. C., Jr., Tremonti, C., A., Dale, D. A., Smith, J.-D. T., & Calzetti, D. 2010, ApJS, 190, 233

Mullan, B., et al. 2011, ApJ, 731, 93

Neff, S. G. & Ulvestad, J. S. 2000, AJ, 120, 670

Noll, S., Burgarella, D., Giovannoli, E., Buat, V., Marcillac, D., & Muñoz-Mateos, J. C. 2009, A&A, 507, 1793

Ohsuga, K. & Mineshige, S. 2011, ApJ, 736, 2011

Owen, R. A. & Warwick, R. S. 2009, MNRAS, 394, 1741

Pahre, M. A., Ashby, M. L. N., Fazio, G. G., & Willner, S. P. 2004, ApJS, 154, 235

Pancoast, A., Sajini, A., Lacy, M., Noriega-Crespo, A., & Rho, J. 2010, ApJ, 723, 530

Peeters, E., Spoon, H. W. W., & Tielens, A. G. G. M. 2004, ApJ, 613, 986

Peterson, B. W., Struck, C., Smith, B. J., & Hancock, M. 2009, MNRAS, 400, 1208

Persic, M., Rephaeli, Y., Braito, V., Cappi, M., Della Ceca, R., Franceschini, A., & Gruber, D. E. 2004, A&A, 419, 849

Popping, G., Pérez, I., & Zurita, A. 2010, A&A, 521, 8

Press, W. H., Teukolsky, S. A., Vetterling, W. T., & Flannery, B. P. 1992, Numerical Recipes in Fortran, Second Edition (Cambridge University Press, Cambridge), p. 692.

Ranalli, P., Comastri, A., & Setti, G. 2003, A&A, 399, 39

Rosenberg, J. L., Ashby, M. L. N., Salzer, J. J., & Huang, J.-S., 2006, ApJ, 636, 742

Rosenberg, J. L., Wu, Y., Le Floch́, E., Charmandaris, V., Ashby, M. L. N., Houck, J. R., Salzer, J. J., & Willner, S. P. 2008, ApJ, 674, 814

Rubin, V. C., Ford, W. K., Jr, & D'Odorico, S. 1970, ApJ, 160, 801

Sanchez, S. F., Rosales-Ortega, F. F., Marino, R. A., et al. 2012, A&A, 546, 2

Saviane, I., Momany, Y., de Costa, G. S., Rich, R. M., & Hibbard, J. E. 2008, ApJ, 678, 179

Schlafly, E. F. & Finkbeiner, D. P. 2011, ApJ, 737, 103

Schweizer, F., Burnes, G. R., Madore, B. F., et al. 2008, AJ, 136, 1482

Silich, S., Tenorio-Tagle, G., & Añorve-Zeferino, G. A. 2005, ApJ, 635, 1116

Sirianna, M., Jee, M. J., Benítez, N., et al. 2005, PASP, 117, 836

Skrutskie, M. F., Cutri, R. M., Stiening, R., et al. 2006, AJ, 131, 1163.

Smith, B. J. & Hancock, M. 2009, AJ, 138, 130

Smith, B. J., Struck, C., Appleton, P. N., Charmandaris, V., Reach, W. & Eitter, J. J. 2005, AJ, 130, 2117

Smith, B. J., Struck, C., Hancock, M., Appleton, P. N., Charmandaris, V. & Reach, W. 2007, AJ, 133, 791

Smith, B. J., Struck, C., Hancock, M., Giroux, M. L., Appleton, P. N., Charmandaris V., Reach, W., Hurlock, S., & Hwang, J. 2008, AJ135, 2406

Smith, B. J., Struck, C., & Nowak, M. A. 2005, AJ, 129, 1350

Smith, B. J., Giroux, M. L., Struck, C., Hancock, M., and Hurlock, S. 2010, AJ, 139, 1212; Erratum 2010, AJ, 139, 2719

Smith, B. J., Swartz, D. A., Miller, O., Burleson, J. A., Nowak, M. A., & Struck, C. 2012, AJ, 143, 144

Snijders, L., van der Werf, P. P., Brandl, B. R., Mengel, S., Schaerer, P., & Wang, Z. 2006, ApJ, 648, L25

Strickland, D. M., Heckman, T. M., Colbert, E. J. M., Hoopes, C. G., & Weaver, K. A. 2004, ApJ, 606, 829

Struck, C., Kaufman, M., Brinks, E., Thomasson, M., Elmegreen, B. G., & Elmegreen, D. M. 2005, MNRAS, 364, 69

Struck, C. & Smith, B. J. 2003, ApJ, 589, 157

Struck, C. & Smith, B. J. 2012, MNRAS, 422, 2444

Sutton, A. D., Roberts, T. P., Walton, D. J., Gladstone, J. C., & Scott, A. E. 2012, MNRAS, 423, 1154

Sutton, A. D., Roberts, T. P., & Walton, D. J. 2011, Astron. Nachr. 332, 362

Swartz, D. A., Ghosh, K. K., Tennant, A. F., & Wu, K. 2004, ApJS, 154, 519

Swartz, D. A., Soria, R., Tennant, A. F., & Yukita, M. 2011, ApJ, 741, 49

Swartz, D. A., Tennant, A. F., & Soria, R. 2009, ApJ, 703, 159

Tammann, G. A. & Reindl, B. 2013, A&A, 549, A136

Teyssier, R., Chapon, D., & Bournaud, F. 2010, ApJ, 720, L149

Toomre, A. & Toomre, J. 1972, ApJ, 178, 623

Trancho, G., Bastian, N., Schweizer, F., & Miller, B.W. 2007, ApJ, 658, 993

Trancho, G., Konstantopoulos, I. S., Bastian, N., Fedotov, K., Gallagher, S., Mullan, B., & Charlton, J. C. 2012, ApJ, 748, 102

Vazquez, G. A., & Leitherer, C. 2005, ApJ, 621, 695

Vila, M. B., Pedlar, A., Davies, R. D., Hummel, E., & Axon, D. J. 1990, MNRAS, 242, 379

Wetzstein, M., Naab, T., & Burket, A. 2007, MNRAS, 375, 805

Whitmore, B. C., et al. 2010, AJ, 140, 75

Whitmore, B. C. & Schweizer, F. 1995, AJ, 109, 960

Whitmore, B. C. & Zhang, Q. 2002, AJ, 124, 1418

Williams, B. F., Binder, B. A., Dalcanton, J. J., Eracleous, M., & Dolphin, A. 2013, ApJ, 772, 12

Wilson, C. D., Petitpas, G. R., Iono, D., et al. 2008, ApJS, 178, 189

Wilson, C. D., Schoville, N., Madden, S., & Charmandaris, V. 2000, ApJ, 542, 120

Wu, Y., et al. 2007, ApJ, 662, 952

Yukita, M., Swartz, D. A., Tennant, A. F., & Soria, R. 2010, AJ, 139, 1066

Zampieri, L. & Roberts, T. P. 2009, MNRAS, 400, 677

Zhang, Q., Fall, S. M., & Whitmore, B. C. 2001, ApJ, 561, 727

Zhang, H.-X., Gao, Y., & Kong, X. 2010, MNRAS, 401, 1839

Zaragoza-Cardiel, J., Font-Serra, J., Beckman, J. E., et al. 2013, MNRAS, 432, 998

Zezas, A. & Fabbiano, G. 2002, ApJ, 577, 726

Zezas, A., Fabbiano, G., Rots, A. H., & Murray, S. S. 2002a, ApJ, 577, 710

Zezas, A., Fabbiano, G., Rots, A. H., & Murray, S. S. 2002a, ApJS, 142, 239

Zezas, A., et al. 2006, ApJS, 166, 211

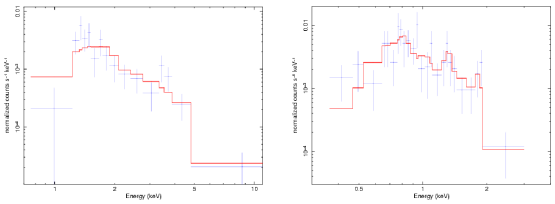

Fig. 1.— Left: The X-ray spectrum of the ULX in Arp 240W (clump 4). The spectrum is well-fitted by a relatively steep power law with a photon index $\gamma = 2.7 \pm {}^{1.0}_{0.8}$ and an absorbing column $N_H \sim 1.5 \times 10^{22}$ cm^{-2}. The small number of counts and the small energy range available for spectral fitting do not allow us to constrain the absorbing column or distinguish between a power-law model and a curved model (eg, a Comptonized disk-blackbody). Right: The X-ray spectrum of the source in Arp 240E. The spectrum is fit with a two-component model, in which the column densities of the two components differ, but the temperatures are the same. The best-fit temperature is $kT = 0.30 \pm {}^{0.09}_{0.07}$ keV. The dominant component is highly absorbed ($N_H = 1.6 \times 10^{22}$ cm^{-2}, while the second is 2×10^{20} cm^{-2}, near the Galactic value.

This 2-column preprint was prepared with the AAS LaTeX macros v5.2.

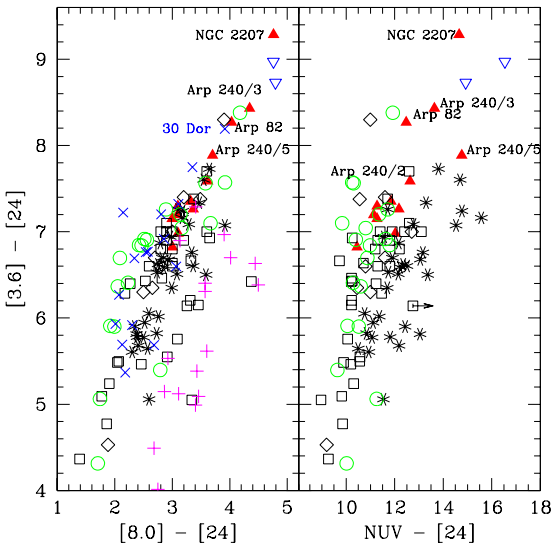

Fig. 2.— UV/IR colors for the hinge clumps in the sample (red filled triangles), compared to knots of star formation in other galaxies. These include: Zhang, Gao, & Kong (2010) regions 3 and 4 in the overlap region of the Antennae (blue upside down open triangles), other star forming knots in the Antennae (black asterisks), regions in NGC 2403 (open green circles), LMC regions (blue crosses), SMC regions (magenta plus signs), and clumps in other interacting galaxies, where the open black squares are disk clumps and the open black diamonds are tail clumps. For clarity, errorbars are omitted. These are generally about the size of the data points or slightly larger. Some of the clumps are labeled. The Spitzer 24 μm data for 30 Doradus in the LMC is saturated, thus the [3.6] − [24] and [8.0] − [24] colors are lower limits.

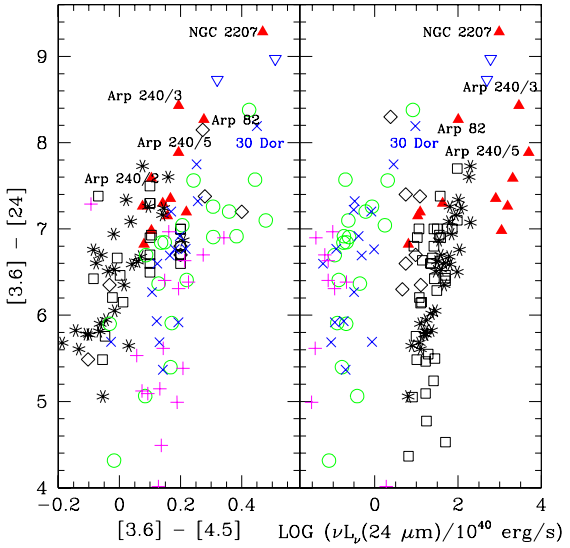

Fig. 3.— Left: The [3.6] − [24] color plotted against [3.6] − [4.5]. Right: The [3.6] − [24] color plotted against $L_{24} = \nu L_\nu$. The hinge clumps are plotted as filled red triangles, regions 3 and 4 in the overlap region of the Antennae are shown as blue upside down open triangles, other star forming knots in the Antennae are black asterisks, regions in NGC 2403 are given as open green circles, LMC regions are blue crosses, SMC regions are magenta plus signs, disk clumps in other interacting galaxies are open black squares, and tail clumps in other systems are black diamonds. Some of the clumps are labeled. The Spitzer 24 μm data for 30 Doradus in the LMC is saturated, thus the [3.6] − [24] color and the 24 μm luminosities are lower limits.

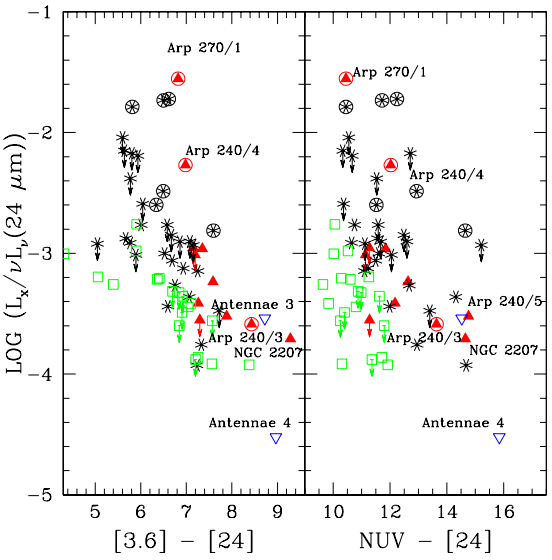

Fig. 4.— Plot of the observed L_X/L_{24} vs. [3.6] − [24] (left panel) and vs. NUV − [24] (right panel) for the eight hinge clumps with Chandra data (red filled triangles), regions 3 and 4 in the Antennae (upside down open blue triangles), other locations in the Antennae (black asterisks), and star forming regions within NGC 2403 (open green squares). These values are *not* corrected for dust attenuation. Points surrounded by circles contain bright X-ray point sources.

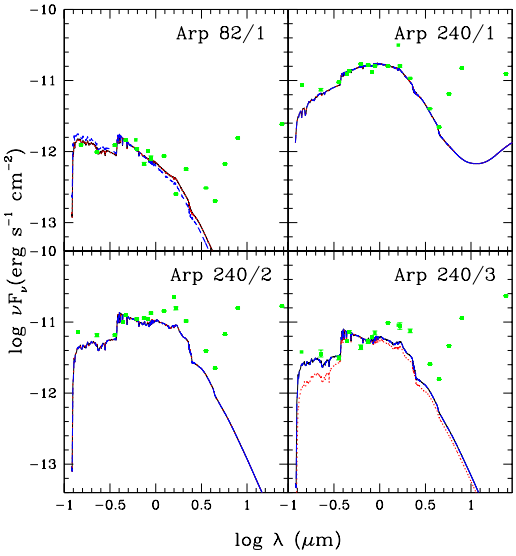

Fig. 5.— Broadband large aperture GALEX/SDSS/Spitzer/HST/2MASS UV/optical/IR spectral energy distributions (SEDs) of some of the clumps in the sample (green filled squares). The black solid curve is the best-fit single-age instantaneous burst model. The blue dashed curve is the burst model with the best-fit reddening, and an age 1σ less than the best fit age. The red dotted curve is the burst model with the best-fit reddening, and an age 1σ more than the best fit age. The plotted error bars only include statistical errors. Note that the fits only include the GALEX/SDSS UV/optical photometry; we extend the model stellar component to longer wavelengths to compare with the Spitzer and near-infrared data to search for excesses in those bands (see Section 7.2).

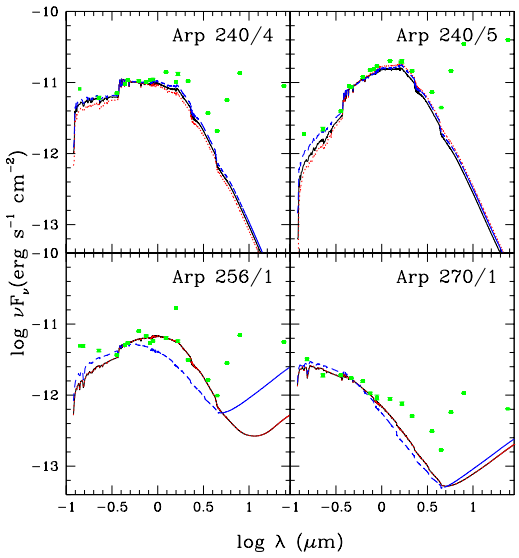

Fig. 6.— Broadband large aperture GALEX/SDSS/Spitzer/HST/2MASS UV/optical/IR spectral energy distributions (SEDs) of some of the clumps in the sample (green filled squares). The black solid curve is the best-fit single-age instantaneous burst model. The blue dashed curve is the burst model with the best-fit reddening, and an age 1σ less than the best fit age. The red dotted curve is the burst model with the best-fit reddening, and an age 1σ more than the best fit age. The plotted error bars only include statistical errors. Note that the fits only include the GALEX/SDSS UV/optical photometry; we extend the model stellar component to longer wavelengths to compare with the Spitzer and near-infrared data to search for excesses in those bands (see Section 7.2).

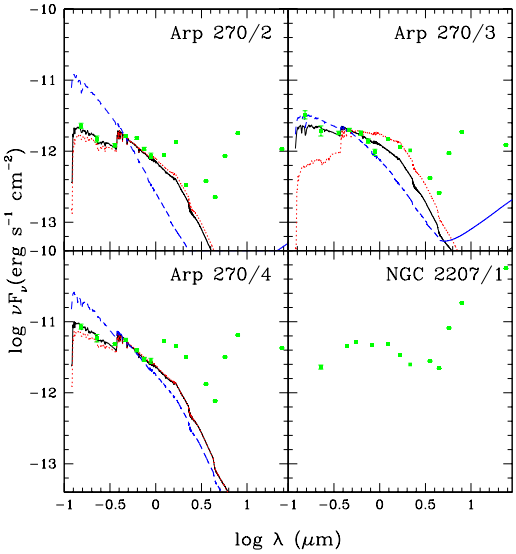

Fig. 7.— Broadband large aperture GALEX/SDSS/Spitzer/HST/2MASS UV/optical/IR spectral energy distributions (SEDs) of some of the clumps in the sample (green filled squares). The black solid curve is the best-fit single-age instantaneous burst model. The blue dashed curve is the burst model with the best-fit reddening, and an age 1σ less than the best fit age. The red dotted curve is the burst model with the best-fit reddening, and an age 1σ more than the best fit age. The plotted error bars only include statistical errors. Note that the fits only include the GALEX/SDSS UV/optical photometry; we extend the model stellar component to longer wavelengths to compare with the Spitzer and near-infrared data to search for excesses in those bands (see Section 7.2). Since no SDSS data is available for NGC 2207, we do not provide a best-fit model for that region.

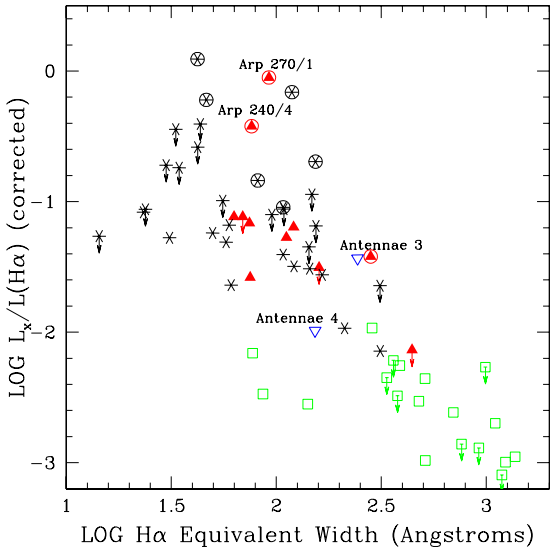

Fig. 8.— A plot of the reddening-corrected $L_X/L_{H\alpha}$ ratio against Hα equivalent width. The hinge clumps are the filled red triangles, the upside down open blue triangles are regions 3 and 4 in the Antennae, the black asterisks are other positions in the Antennae, and the open green squares are regions within NGC 2403. For this plot, the reddening correction was determined from the $L_{24}/L_{H\alpha}$ ratio as described in the text. The symbols enclosed in circles represent regions with strong X-ray point sources.

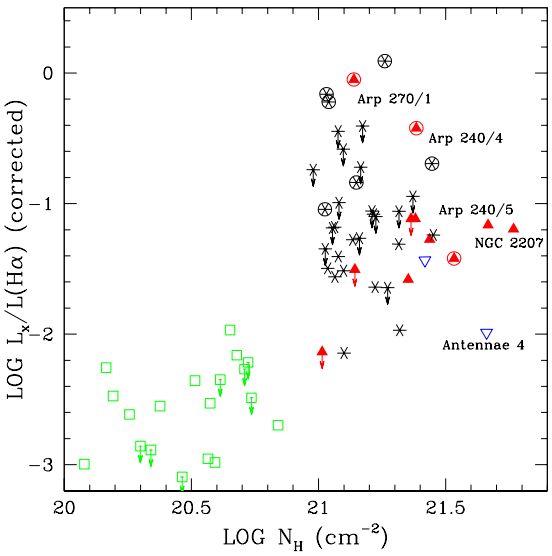

Fig. 9.— A plot of the reddening-corrected $L_X/L_{H\alpha}$ ratio against hydrogen column density, both determined using the $L_{24}/L_{H\alpha}$ ratio as described in the text. The hinge clumps are the filled red triangles, the upside down open blue triangles are regions 3 and 4 in the Antennae, the black asterisks are other positions in the Antennae, and the open green squares are regions within NGC 2403. The symbols enclosed in circles represent regions with strong X-ray point sources.

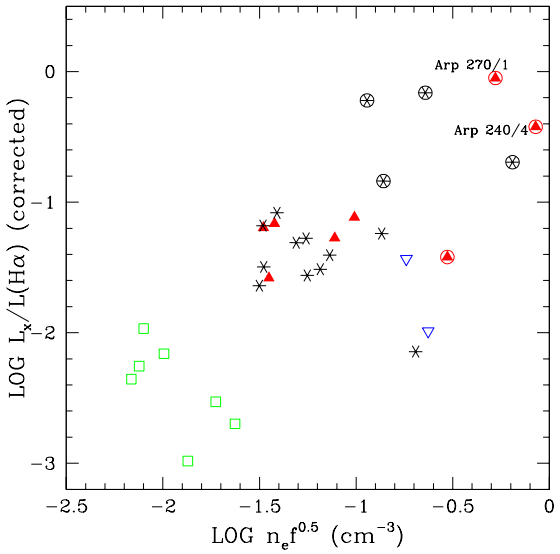

Fig. 10.— A plot of the reddening-corrected $L_X/L_{H\alpha}$ ratio against electron number density n_e $\times$ $\sqrt{f}$, where f is the volume filling factor. The hinge clumps are the filled red triangles, the upside down open blue triangles are regions 3 and 4 in the Antennae, the black asterisks are other positions in the Antennae, and the open green squares are regions within NGC 2403. The symbols enclosed in circles represent regions with strong X-ray point sources; if these are ULXs, the derived n_e are not relevant.

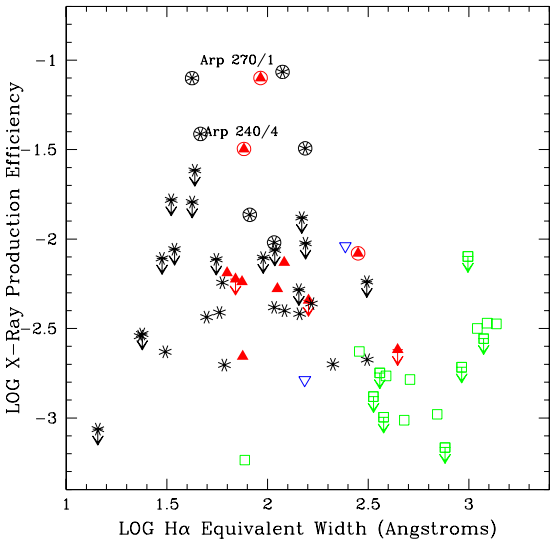

Fig. 11.— A plot of X-ray production efficiency = L_X/L_{mech} vs. Hα equivalent width. The hinge clumps are the filled red triangles, the upside down open blue triangles are regions 3 and 4 in the Antennae, the black asterisks are other positions in the Antennae, and the open green squares are regions within NGC 2403. The symbols enclosed in circles represent regions containing strong X-ray point sources.

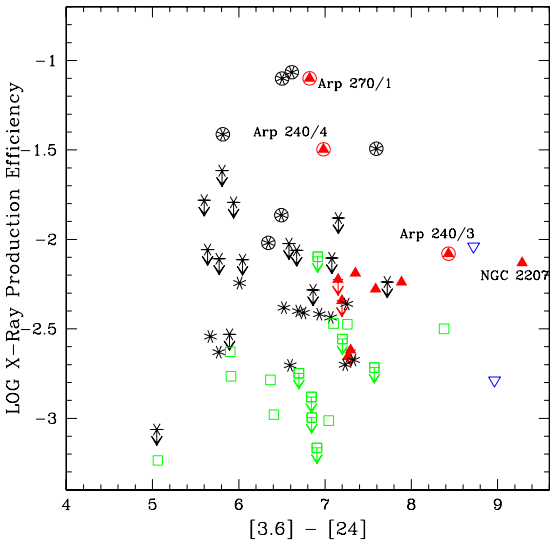

Fig. 12.— A plot of X-ray production efficiency = L_X/L_{mech} against the [3.6] − [24] color. The hinge clumps are the filled red triangles, while open blue upside down triangles are regions 3 and 4 in the Antennae, the black asterisks are other positions in the Antennae, and the open green squares are regions within NGC 2403. The symbols enclosed in circles represent regions containing strong X-ray point sources. The reddest hinge clump in [3.6] - [24] is NGC 2207; the second reddest is Arp 240-3.

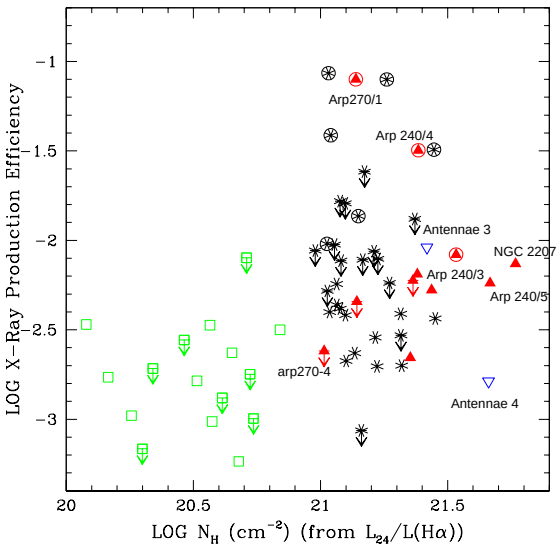

Fig. 13.— A plot of X-ray production efficiency = L_X/L_{mech} vs. N_H, where N_H was calculated from the $L_{24}/L_{H\alpha}$ ratio, with the assumptions given in the text. The hinge clumps are the filled red triangles, while open blue upside down triangles are regions 3 and 4 in the Antennae, the black asterisks are other positions in the Antennae, and the open green squares are regions within NGC 2403. The symbols enclosed in circles represent regions containing strong X-ray point sources.

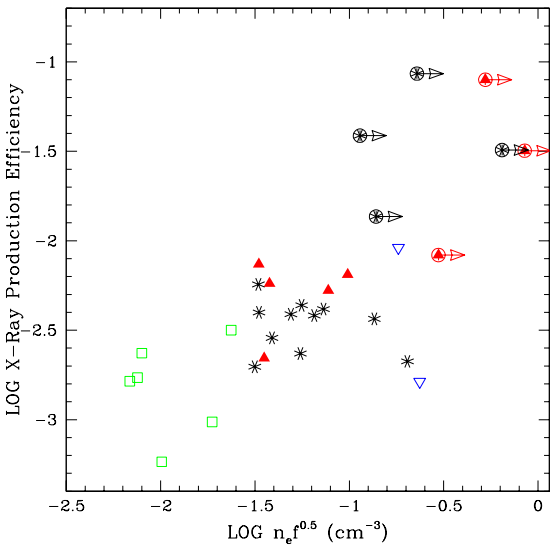

Fig. 14.— A plot of X-ray production efficiency = L_X/L_{mech} vs. electron density $n_e \times \sqrt{(f)}$, where f is the volume filling factor. The hinge clumps are the filled red triangles, while open blue upside down triangles are regions 3 and 4 in the Antennae, the black asterisks are other positions in the Antennae, and the open green squares are regions within NGC 2403. The symbols enclosed in circles and marked by lower limit symbols represent regions containing strong X-ray point sources. These may be ULXs, for which the estimate of n_e is not valid.

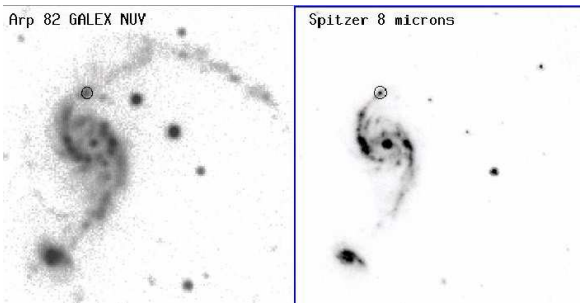

Fig. 15.— Left panel: GALEX NUV image of Arp 82. Right panel: Spitzer 8 μm image of Arp 82. The field of view is 4.′5 × 4.′5. North is up and east to the left. The northern hinge clump is marked by a circle with a radius of 5″. Note the ocular ('eye-shaped') morphology of the northern galaxy. The northern tail is much more evident in the NUV image than in the mid-infrared.

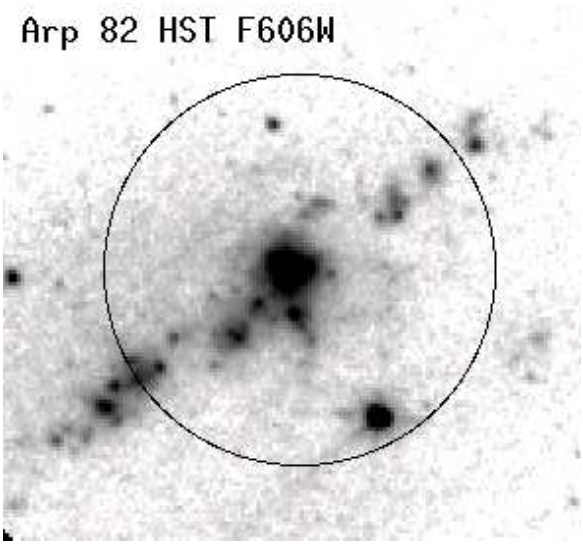

Fig. 16.— The archival HST F606W image of the region around the hinge clump. A 5″ radius circle is plotted marking the hinge clump. Note the luminous source in the center of a straight line of fainter star clusters. The HST archival images of Arp 82 were included in the Mullan et al. (2011) large statistical study of the frequency of clusters in tidal features, however, their study did not present any analysis of individual clusters or cluster associations. No Chandra data is available for Arp 82.

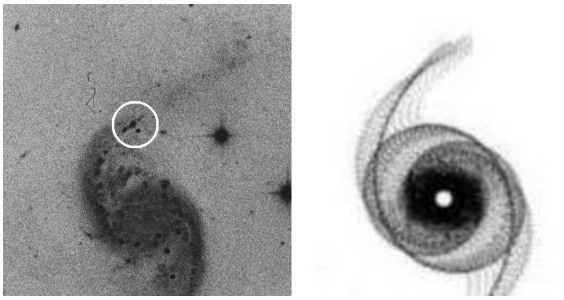

Fig. 17.— Left: a close-up view of the Arp (1966) Atlas optical photograph of the hinge region in NGC 2535 (the northern galaxy in Arp 82). The hinge clump is marked. Right: an analytical model of a prolonged prograde interaction from Struck & Smith (2012). See text for more details.

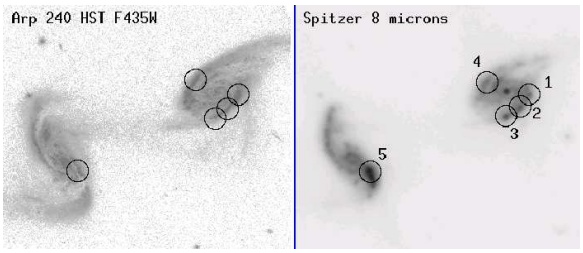

Fig. 18.— Left panel: The HST F435W image of Arp 240. Right panel: The Spitzer 8 μm image of Arp 240. North is up and east to the left. The field of view is $1\farcm7 \times 2\farcm1$. The five hinge clumps are marked with $5''$ radii and labeled. The HST images of Arp 240 were previously used by Haan et al. (2011) to extract nuclear profiles, but no analysis of the non-nuclear clusters was done.

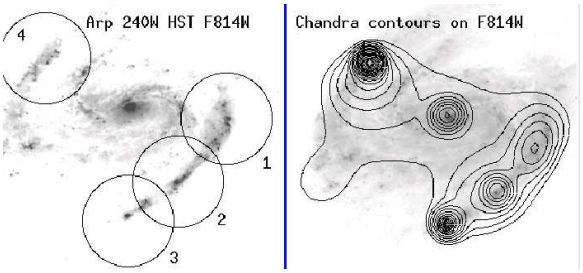

Fig. 19.— Left: A closer view of the HST F814W image of Arp 240W, with the greyscale set to emphasize the small-scale structure. Right: A smoothed Chandra $0.3 - 8$ keV map of Arp 240W plotted as contours on the HST F814W map. In the left panel, the sample hinge clumps are marked by circles with radii of $5''$ and are labeled. The field of view is $30'' \times 33''$. North is up and east to the left.

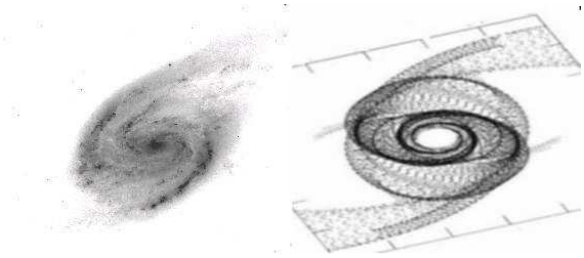

Fig. 20.— Left: The HST F814W image of Arp240W. Right: An analytical model from Struck & Smith (2012) that approximates the structure of Arp 240W (see text for details).

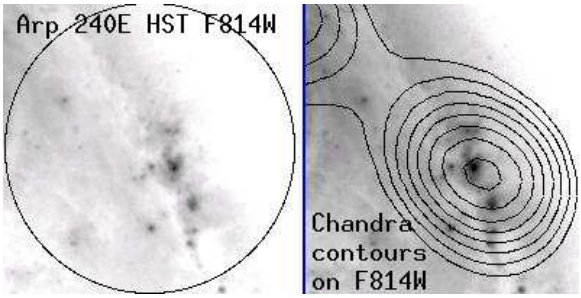

Fig. 21.— Left: A closer view of the HST F814W image of the hinge clump in Arp 240E (clump 5). The hinge clump is marked by a 5″ radius circle. Right: The smoothed $0.3 - 8$ keV Chandra map of Arp 240E. North is up and east to the left. Notice the strong and spatially extended X-ray emission from this source ($L_X = 1.4 \times 10^{41}$ erg s^{-1} after correction for internal extinction). The HST image shows an extremely luminous source near this location ($M_I = -16.5$ with $\leq$75 pc diameter.)

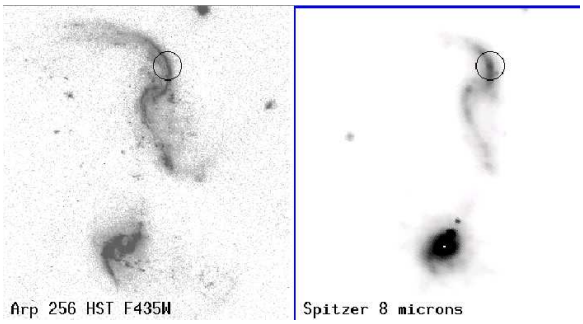

Fig. 22.— Arp 256. Left: HST F435W image. Right: Spitzer 8 μm image. The field of view is $1\farcm67 \times 1\farcm8$. North is up and east to the left. The hinge clump in the northern tail is marked. Note the tidal dwarf galaxy in the southern tail of the northern galaxy.

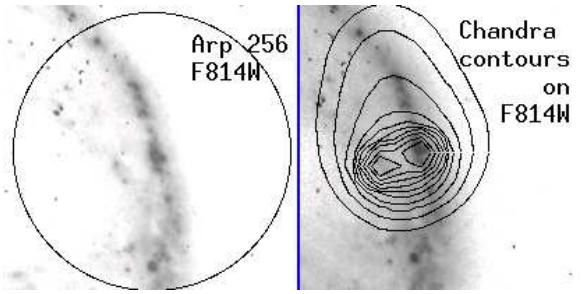

Fig. 23.— Left: A close-up view of the HST F814W image of Arp 256N. A 5″ radius encircling the hinge clump is marked. Note the flattened structure of the bright source near the center of the hinge clump. Right: The smoothed 0.3 − 8 keV Chandra image of the same region, plotted as contours on the F814W image.

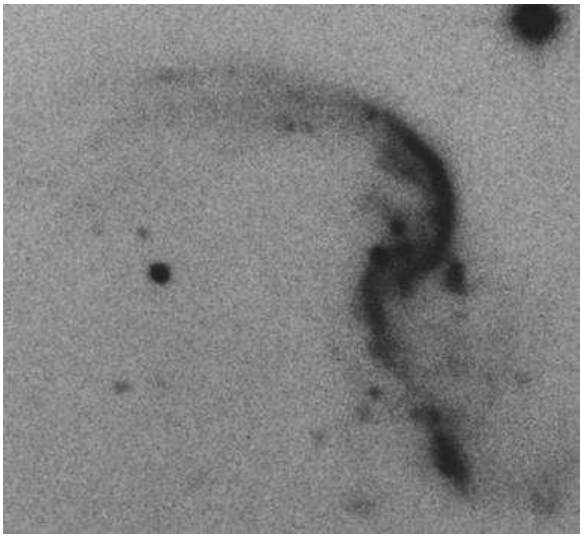

Fig. 24.— A close-up view of the Arp (1966) Atlas image of Arp 256N. The northern tail appears double. The 'X' shape in the center of the galaxy is due to star formation outside of the main disk of the galaxy (see Figure 25).

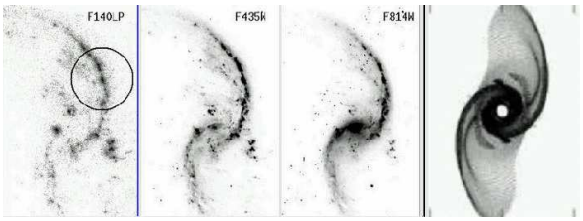

Fig. 25.— A comparison of the HST UV/optical images of Arp 256N (left three panels) with an analytical model from Struck & Smith (2012). See text for more details on the model.

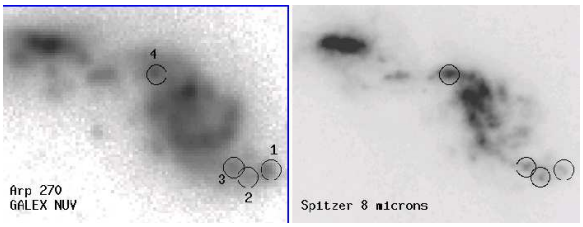

Fig. 26.— Arp 270. Left: GALEX NUV image. Right: Spitzer 8 μm image. The field of view is $1\farcm9 \times 2\farcm5$. North is up and east to the left. The four targeted clumps are marked and labeled. NGC 3396 is the galaxy to the east (left), while NGC 3395 is to the west.

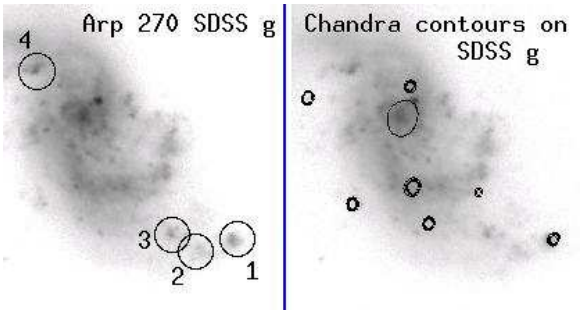

Fig. 27.— Left: A close-up view of the SDSS g image of Arp 270, with the targeted clumps marked and labeled. Right: The SDSS g image with the smoothed 0.3 − 8 keV Chandra image superimposed as contours. The field of view is 1.′1 × 1.′2.

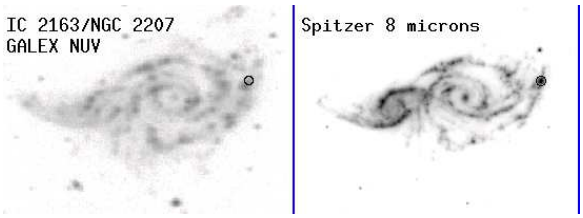

Fig. 28.— The IC 2163/NGC 2207 interacting galaxy pair. Left: The GALEX NUV image. Right: The Spitzer 8 micron image. North is up and east to the left. The field of view is 4.′0 × 6.′7. NGC 2207 is the galaxy to the west (right) in this picture. The hinge clump is marked by a circle with a 5″ radius.

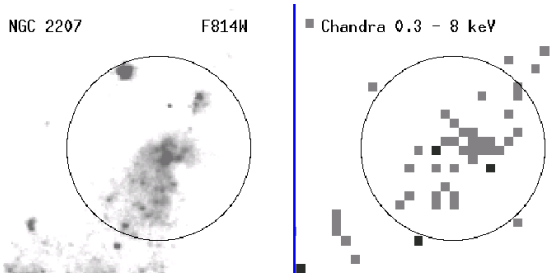

Fig. 29.— A closer view of the NGC 2207 hinge clump. Left: The HST F814W image. Right: The unsmoothed Chandra 0.3 − 8 keV image. The circle has a 5″ radius. North is up and east to the left.

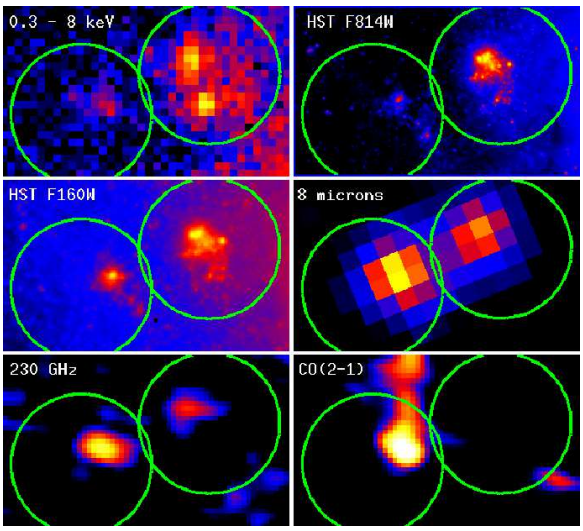

Fig. 30.— A multi-wavelength montage of the overlap region of the Antennae. Upper left: the co-added 0.3 − 8 keV Chandra map. Upper right: an archival HST ACS F814W optical image. Middle left: an archival HST WFC3 F160W near-infrared image. Middle right: the 8 μm Spitzer image. Lower left: an ALMA 230 GHz continuum map. Lower right: an ALMA CO(2-1) map. North is up and east to the left. The left and right circles are Zhang, Gao, & Kong (2010) regions 4 and 3, respectively, with radii of 4.″5. The brightest cluster in region 4 is known as WS80 (source 80 from Whitmore & Schweizer 1995), while the bright complex of star clusters in region 3 is called Knot B (Rubin et al. 1970; Whitmore et al. 2010). The spatial resolution of the ALMA maps is 1.″68 × 0.″85.

TABLE 1
HINGE CLUMP SAMPLE

Clump	RA (J2000)	Dec. (J2000)	Distance* (Mpc)	GALEX? (NUV/FUV)	SDSS?
Arp 82-1	08 11 13.9	+25 13 09.6	59.2	yy	y
Arp 240-1	13 39 52.3	+00 50 22.8	101.7	yn	y
Arp 240-2	13 39 52.5	+00 50 17.3	101.7	yn	y
Arp 240-3	13 39 53.0	+00 50 12.9	101.7	yn	y
Arp 240-4	13 39 53.6	+00 50 28.6	101.7	yn	y
Arp 240-5	13 39 57.2	+00 49 46.8	101.7	yn	y
Arp 256-1	00 18 49.8	−10 21 33.8	109.6	yy	y
Arp 270-1	10 49 46.6	+32 58 23.9	29.0	yy	y
Arp 270-2	10 49 47.5	+32 58 20.3	29.0	yy	y
Arp 270-3	10 49 48.1	+32 58 25.2	29.0	yy	y
Arp 270-4	10 49 51.2	+32 59 11.7	29.0	yy	y
NGC 2207-1	06 16 15.9	−21 22 02.6	38.0	yn	n

*Distances from the NASA Extragalactic Database, assuming H_0 = 73 km s^{-1} Mpc^{-1}, and accounting for peculiar velocities due to the Virgo Cluster, the Great Attractor, and the Shapley Supercluster.

Table 2
Hubble Space Telescope Data

Galaxy	Instrument(s)	Filters	Observing Time (Seconds)
Arp 82	WFPC2	F606W	1900
		F814W	1900
Arp 240	ACS	F140LP	2516
		F435W	1260
		F814W	720
Arp 240E	WFC3	F160W	2395
Arp 240W	NICMOS	F160W	2303
Arp 256	ACS	F140LP	2520
		F435W	1260
		F814W	720
	NICMOS	F160W	2495
NGC 2207	WFPC2	F439W	2000
		F555W	660
		F814W	720

Table 3
Chandra Telescope Data

Galaxy	Dataset	Exposure Time (ksec)
Arp 240	10565	19.9
Arp 256	13823	29.5
Arp 270	2042	19.3
NGC 2207	14914	12.9

Table 4
GALEX Aperture Corrections

Galaxy	Filter	Aperture Correction	Filter	Aperture Correction
Arp 82	NUV	1.19 ± 0.04	FUV	1.23 ± 0.15
Arp 240	NUV	1.23 ± 0.08		
Arp 256	NUV	1.30 ± 0.11	FUV	1.46 ± 0.07
Arp 270	NUV	1.16 ± 0.02	FUV	1.41 ± 0.31
NGC 2207	NUV	1.24 ± 0.05		

*Multiplicative Aperture Corrections, for a 5″ radius aperture.

Table 5

Large Aperture GALEX/SDSS/Spitzer Magnitudes for Sample Hinge Clumps

Clump	FUV (mag)	NUV (mag)	u (mag)	g (mag)	r (mag)	i (mag)	z (mag)	3.6 μm (mag)	4.5 μm (mag)	5.8 μm (mag)	8.0 μm (mag)	24 μm (mag)
Arp 82-1	19.19 ± 0.02	19.02 ± 0.02	18.37 ± 0.03	17.92 ± 0.01	17.94 ± 0.03	18.29 ± 0.05	17.92 ± 0.08	14.71 ± 0.01	14.43 ± 0.01	12.40 ± 0.01	10.47 ± 0.01	6.44 ± 0.01
Arp 240-1	–	16.82 ± 0.04	16.16 ± 0.01	15.47 ± 0.02	14.97 ± 0.02	14.80 ± 0.02	14.67 ± 0.03	11.92 ± 0.01	11.84 ± 0.01	9.93 ± 0.01	8.02 ± 0.01	4.65 ± 0.02
Arp 240-2	–	16.97 ± 0.05	16.56 ± 0.03	15.59 ± 0.02	15.44 ± 0.03	15.22 ± 0.03	14.88 ± 0.03	11.93 ± 0.01	11.83 ± 0.01	9.90 ± 0.01	7.96 ± 0.01	4.35 ± 0.02
Arp 240-3	–	17.61 ± 0.12	17.35 ± 0.07	16.18 ± 0.04	16.44 ± 0.08	16.04 ± 0.07	15.57 ± 0.07	12.41 ± 0.01	12.21 ± 0.01	10.29 ± 0.01	8.32 ± 0.01	3.98 ± 0.01
Arp 240-4	–	17.04 ± 0.06	16.48 ± 0.02	15.74 ± 0.02	15.49 ± 0.03	15.35 ± 0.04	15.08 ± 0.04	12.00 ± 0.01	11.90 ± 0.01	10.08 ± 0.01	8.12 ± 0.01	5.02 ± 0.01
Arp 240-5	–	18.14 ± 0.06	17.11 ± 0.03	15.97 ± 0.03	15.37 ± 0.03	14.93 ± 0.03	14.61 ± 0.03	11.27 ± 0.01	11.08 ± 0.01	9.05 ± 0.01	7.09 ± 0.01	3.39 ± 0.01
Arp 256-1	17.71 ± 0.04	17.44 ± 0.04	17.18 ± 0.02	16.49 ± 0.02	15.80 ± 0.02	15.76 ± 0.02	15.78 ± 0.03	12.88 ± 0.01	12.72 ± 0.01	10.84 ± 0.01	8.85 ± 0.01	5.53 ± 0.01
Arp 270-1	18.18 ± 0.04	18.31 ± 0.06	17.90 ± 0.03	17.72 ± 0.02	17.57 ± 0.03	17.80 ± 0.04	17.77 ± 0.08	14.71 ± 0.01	14.62 ± 0.01	12.57 ± 0.01	10.89 ± 0.01	7.88 ± 0.02
Arp 270-2	18.54 ± 0.09	18.57 ± 0.11	18.39 ± 0.06	17.80 ± 0.04	17.60 ± 0.04	17.77 ± 0.05	17.85 ± 0.10	14.48 ± 0.02	14.32 ± 0.02	12.13 ± 0.01	10.33 ± 0.01	7.33 ± 0.03
Arp 270-3	18.16 ± 0.14	18.29 ± 0.18	17.95 ± 0.06	17.57 ± 0.06	17.42 ± 0.07	17.50 ± 0.08	17.73 ± 0.11	14.37 ± 0.02	14.15 ± 0.02	12.04 ± 0.02	10.27 ± 0.01	7.18 ± 0.03
Arp 270-4	17.11 ± 0.09	17.08 ± 0.13	16.89 ± 0.04	16.47 ± 0.06	16.56 ± 0.05	16.68 ± 0.07	16.56 ± 0.09	13.12 ± 0.01	12.98 ± 0.01	10.71 ± 0.01	8.92 ± 0.01	5.83 ± 0.01
NGC 2207-1	–	18.10 ± 0.07	–	–	–	–	–	12.31 ± 0.01	11.84 ± 0.01	9.69 ± 0.01	7.79 ± 0.01	3.03 ± 0.01

*Zero magnitude flux densities are 3631 Jy for the GALEX and SDSS bands, and 277.5 Jy, 179.5 Jy, 116.6 Jy, 63.1 Jy, and 7.3 Jy for 3.6 μm, 4.5 μm, 5.8 μm, 8.0 μm, and 24 μm, respectively.

Table 6
Hα and 2MASS Photometry

Clump	$L_{H\alpha}$ (erg/s) (observed)	Hα EW (Å)	J (mag)	H (mag)	K (mag)
Arp 82-1	$2.2 \pm 0.7 \times 10^{40}$	342.2 ± 102.7	16.62 ± 0.08	17.18 ± 0.3	15.54 ± 0.11
Arp 240-1	$25.4 \pm 7.6 \times 10^{40}$	75.2 ± 22.6	13.46 ± 0.06	12.68 ± 0.07	12.34 ± 0.07
Arp 240-2	$23.8 \pm 7.2 \times 10^{40}$	111.8 ± 33.6	13.57 ± 0.07	12.71 ± 0.07	12.38 ± 0.07
Arp 240-3	$21.4 \pm 6.4 \times 10^{40}$	281.8 ± 84.6	13.99 ± 0.11	13.33 ± 0.13	12.72 ± 0.1
Arp 240-4	$16 \pm 4.8 \times 10^{40}$	76.4 ± 22.9	13.6 ± 0.08	12.88 ± 0.08	12.37 ± 0.07
Arp 240-5	$17.4 \pm 5.2 \times 10^{40}$	74.6 ± 22.4	13.2 ± 0.06	12.44 ± 0.07	12.0 ± 0.06
Arp 256-1	$11.8 \pm 3.5 \times 10^{40}$	63 ± 18.9	14.45 ± 0.06	13.79 ± 0.07	13.66 ± 0.08
Arp 270-1	$0.2 \pm 0.1 \times 10^{40}$	92.3 ± 27.7	16.59 ± 0.13	15.98 ± 0.17	15.66 ± 0.17
Arp 270-2	$0.2 \pm 0.1 \times 10^{40}$	69.3 ± 20.8	16.59 ± 0.13	15.36 ± 0.1	16.1 ± 0.28
Arp 270-3	$0.4 \pm 0.1 \times 10^{40}$	159.9 ± 48	16.05 ± 0.12	15.55 ± 0.16	14.88 ± 0.11
Arp 270-4	$2.2 \pm 0.7 \times 10^{40}$	443.3 ± 133	14.65 ± 0.13	14.04 ± 0.13	13.66 ± 0.12
NGC 2207-1	$1.7 \pm 0.5 \times 10^{40}$	121.1 ± 36.3	14.77 ± 0.13	14.35 ± 0.13	13.92 ± 0.1

Table 7
Small Aperture HST Photometry for Sample Hinge Clumps[a]

Clump	F140LP	F435W	F439W	F555W	F606W	F814W	F160W
Arp 82-1	···	···	···	···	21.13 ± 0.70	7.84 ± 0.21	···
Arp 240-1	295.89 ± 2.36	45.63 ± 0.49	···	···	···	8.61 ± 0.14	5.88 ± 0.85
Arp 240-2	273.69 ± 3.22	68.16 ± 1.48	···	···	···	20.47 ± 0.40	42.55 ± 1.13
Arp 240-3	229.81 ± 0.94	62.98 ± 0.42	···	···	···	16.76 ± 0.19	19.49 ± 1.01
Arp 240-4	360.35 ± 1.89	37.57 ± 0.58	···	···	···	7.26 ± 0.19	8.11 ± 0.37
Arp 240-5	149.54 ± 0.58	158.76 ± 1.09	···	···	···	50.06 ± 0.78	14.57 ± 0.82
Arp 256-1	267.53 ± 1.99	42.61 ± 0.84	···	···	···	8.38 ± 0.24	6.30 ± 0.39
NGC 2207-1	···	···	12.69 ± 0.55	8.49 ± 0.55	···	7.49 ± 0.56	···

[a]These fluxes were obtained using a $0\farcs15$ radius, and aperture corrections have been applied (see text). All fluxes are in units of 10^{-18} erg s^{-1} cm^{-2} Å^{-1}, and have been corrected for Galactic extinction as described in the text.

Table 8
Large Aperture HST Photometry for Sample Hinge Clumps[a]

Clump	F140LP	F435W	F439W	F555W	F606W	F814W	F160W
Arp 82-1	···	···	···	···	2.65 ± 0.01	1.34 ± 0.01	···
Arp 240-1	73.86 ± 0.01	33.13 ± 0.01	···	···	···	17.29 ± 0.01	20.09 ± 0.07
Arp 240-2	61.92 ± 0.01	26.90 ± 0.01	···	···	···	14.35 ± 0.01	14.55 ± 0.06
Arp 240-3	32.22 ± 0.01	14.19 ± 0.01	···	···	···	8.07 ± 0.01	5.76 ± 0.06
Arp 240-4	69.16 ± 0.01	25.36 ± 0.01	···	···	···	13.93 ± 0.01	6.47 ± 0.11
Arp 240-5	16.08 ± 0.01	23.34 ± 0.02	···	···	···	20.34 ± 0.01	12.39 ± 0.01
Arp 256-1	44.42 ± 0.01	13.02 ± 0.01	···	···	···	6.99 ± 0.01	10.59 ± 0.02
NGC 2207-1	···	···	13.88 ± 0.03	9.30 ± 0.01	···	7.27 ± 0.01	···

[a]These fluxes are all within a $5''$ radius. All fluxes are in units of 10^{-16} erg s^{-1} cm^{-2} Å^{-1}, and have been corrected for Galactic extinction as described in the text.

Table 9
Chandra Results

Clump	R.A.[†] (J2000)	Dec.[†] (J2000)	Background-Subtracted Counts	Flux[*] (erg/s/cm^2) (0.3 − 8 keV)	size[**] ($''$)	L_X[***] (erg/s) (0.3 − 8 keV)	L_X[‡] (erg/s) (0.3 − 8 keV)
Arp 240-1	$13^h39^m52.28^s$	$+00°50'21.''1$	29	3.2×10^{-15}	1.5×3.5	1.5×10^{40}	2.2×10^{40}
Arp 240-2	$13^h39^m52.59^s$	$+00°50'15.''6$	18	3.2×10^{-15}	1.5×1.5	1.8×10^{40}	5.4×10^{40}
Arp 240-3	$13^h39^m52.95^s$	$+00°50'12.''5$	17	4×10^{-15}	$\leq 0.75 \times 0.75$	3.3×10^{40}	5.0×10^{40}
Arp 240-4	$13^h39^m53.51^s$	$+00°50'30.''0$	99	39×10^{-15}	$\leq 0.65 \times 0.65$	17.8×10^{40}	21.9×10^{40}
Arp 240-5	$13^h39^m57.14^s$	$+00°49'46.''6$	86	12.1×10^{-15}	4.8×4.8	14.2×10^{40}	14.2×10^{40}
Arp 256-1	$00^h18^m49.84^s$	$-10°21'34.''5$	42	6.1×10^{-15}	2.0×1.0	3.2×10^{40}	3.2×10^{40}
Arp 270-1	$10^h49^m46.60^s$	$+32°58'23.''7$	50	15×10^{-15}	$\leq 0.85 \times 0.85$	0.4×10^{40}	0.4×10^{40}
Arp 270-2	···	···	≤ 6	$\leq 1.2 \times 10^{-15}$	···	$\leq 0.4 \times 10^{39}$	$\leq 0.4 \times 10^{39}$
Arp 270-3	···	···	≤ 6	$\leq 1.5 \times 10^{-15}$	···	$\leq 0.4 \times 10^{39}$	$\leq 0.3 \times 10^{39}$
Arp 270-4	···	···	≤ 6	$\leq 1.4 \times 10^{-15}$	···	$\leq 0.3 \times 10^{39}$	$\leq 0.3 \times 10^{39}$
NGC 2207-1	$16^h16^m15.5^s$	$-21°22'02.''6$	26	11×10^{-15}	10×6	2.5×10^{40}	2.5×10^{40}

[†]Coordinates of central Chandra source.

[*]Observed flux from source in center of clump.

[**]Approximate total angular extent of X-ray emission from central source within clump.

[***]X-ray luminosity of the central source within the clump; corrected for internal extinction using estimates made from the $L_{H\alpha}/L_{24}$ ratio as described in the text.

[‡]X-ray luminosity within a $5''$ radius aperture. Corrected for internal extinction using estimates made from the $L_{H\alpha}/L_{24}$ ratio as described in the text.

Table 10
Star Formation Rates of the Hinge Clumps

Clump	L_{NUV}[a] (erg/s) (observed)	L_{24}[b] (erg/s) (observed)	SFR[c] ($M_\odot$/yr)	percent[c,d] Global SFR	SFR[e] ($M_\odot$/yr)	percent[d,e] Global SFR
Arp 82-1	5.5×10^{41}	10.2×10^{41}	0.29	7%	0.18	5%
Arp 240-1	109.9×10^{41}	155.4×10^{41}	4.04	19%	3.06	18%
Arp 240-2	96×10^{41}	206.5×10^{41}	4.83	22%	3.73	22%
Arp 240-3	53.4×10^{41}	290.0×10^{41}	6.11	28%	4.7	28%
Arp 240-4	89.8×10^{41}	110.7×10^{41}	2.76	13%	2.25	13%
Arp 240-5	32.5×10^{41}	498.3×10^{41}	9.45	56%	7.69	55%
Arp 256-1	76.9×10^{41}	80.4×10^{41}	2.01	43%	1.71	40%
Arp 270-1	2.2×10^{41}	0.6×10^{41}	0.02	1%	0.02	1%
Arp 270-2	1.8×10^{41}	1.1×10^{41}	0.02	1%	0.02	1%
Arp 270-3	2.3×10^{41}	1.2×10^{41}	0.04	2%	0.03	1%
Arp 270-4	6.9×10^{41}	4.3×10^{41}	0.19	8%	0.11	5%
NGC 2207-1	7×10^{41}	97.1×10^{41}	1.74	24%	1.5	22%

[a]using $L_{NUV} = \nu L_\nu$.

[b]using $L_{24} = \nu L_\nu$.

[c]Calculated using SFR ($M_\odot$/yr) = $5.5 \times 10^{-42}[L_{H\alpha} + 0.031\ L_{24}]$ (erg/s) (Kennicutt et al. 2009).

[d]Percent of total SFR from parent galaxy in the target clump.

[e]Calculated using $L_{NUV}(\mathrm{corr}) = L_{NUV} + 2.26 L_{24}$ and log(SFR) = log(L_{NUV}(corr)) - 43.17 (Hao et al. 2011).

Table 11
Broadband UV/Optical Single-Age Instantaneous Burst Models

Clump	Age (Myr)	E(B-V) (mag)	Stellar Mass ($M_\odot$)	Reduced Chi Squared (χ^2/(N−2))	Colors Used
Arp 82-1	$100 \pm {}^{1}_{21}$	$0.00 \pm {}^{0.06}_{0.00}$	2.5×10^7	11.5	FUV-NUV, NUV-g, u-g, g-r, r-i, i-z
Arp 240-1	$6 \pm {}^{1}_{1}$	$0.54 \pm {}^{0.04}_{0.06}$	45.1×10^7	10.9	NUV-g, u-g, g-r, r-i, i-z
Arp 240-2	$150 \pm {}^{1}_{1}$	$0.14 \pm {}^{0.06}_{0.06}$	203.3×10^7	6.8	NUV-g, u-g, g-r, r-i, i-z
Arp 240-3	$150 \pm {}^{101}_{1}$	$0.14 \pm {}^{0.10}_{0.14}$	95.5×10^7	14.0	NUV-g, u-g, g-r, r-i, i-z
Arp 240-4	$45 \pm {}^{11}_{6}$	$0.28 \pm {}^{0.06}_{0.06}$	111.0×10^7	2.3	NUV-g, u-g, g-r, r-i, i-z
Arp 240-5	$70 \pm {}^{31}_{26}$	$0.56 \pm {}^{0.12}_{0.10}$	338.4×10^7	4.3	NUV-g, u-g, g-r, r-i, i-z
Arp 256-1	$6 \pm {}^{1}_{2}$	$0.54 \pm {}^{0.22}_{0.06}$	21.8×10^7	32.8	FUV-NUV, NUV-g, u-g, g-r, r-i, i-z
Arp 270-1	$5 \pm {}^{1}_{2}$	$0.28 \pm {}^{0.12}_{0.06}$	0.2×10^7	7.1	FUV-NUV, NUV-g, u-g, g-r, r-i, i-z
Arp 270-2	$70 \pm {}^{31}_{67}$	$0.00 \pm {}^{0.58}_{0.00}$	0.7×10^7	1.0	FUV-NUV, NUV-g, u-g, g-r, r-i, i-z
Arp 270-3	$6 \pm {}^{90}_{2}$	$0.26 \pm {}^{0.20}_{0.26}$	0.2×10^7	1.3	FUV-NUV, NUV-g, u-g, g-r, r-i, i-z
Arp 270-4	$50 \pm {}^{21}_{45}$	$0.00 \pm {}^{0.28}_{0.00}$	1.7×10^7	0.6	FUV-NUV, NUV-g, u-g, g-r, r-i, i-z

Table 12
Reddening and Ages from the Hα Data, and Related Quantities

clump	A_V[a] (mag)	E(B−V)[b] (mag)	N_H[c] (10^{21} cm^{-2})	Age[d] (Myrs)	Stellar[e] Mass ($M_\odot$)	$L_X/L_{H\alpha}$[f] (corrected)	L_X/SFR[g] ((erg/s)/($M_\odot$/yr)) (corrected)	$n_e\sqrt{f}$[h] (cm^{-3})	XPE[i]
Arp 82-1	1.34 ± 0.02	0.33 ± 0.01	1.93 ± 0.02	$5.4 \pm {}^{0.2}_{0.0}$	0.7×10^7	...	...	...	...
Arp 240-1	1.59 ± 0.02	0.39 ± 0.01	2.27 ± 0.02	$6.1 \pm {}^{0.5}_{0.0}$	35.2×10^7	0.026	4.1×10^{39}	0.035	0.0022
Arp 240-2	1.93 ± 0.02	0.48 ± 0.01	2.76 ± 0.02	$5.8 \pm {}^{0.3}_{0.0}$	27.5×10^7	0.053	4.2×10^{39}	0.077	0.0053
Arp 240-3	2.41 ± 0.02	0.59 ± 0.01	3.45 ± 0.02	$5.5 \pm {}^{0.1}_{0.0}$	25.7×10^7	0.038	6.2×10^{39}	0.297	0.0083
Arp 240-4	1.71 ± 0.02	0.42 ± 0.01	2.45 ± 0.02	$6.1 \pm {}^{0.5}_{0.0}$	22.0×10^7	0.378	70.9×10^{39}	0.850	0.0319
Arp 240-5	3.27 ± 0.02	0.81 ± 0.01	4.69 ± 0.02	$6.1 \pm {}^{0.5}_{0.0}$	63.0×10^7	0.069	16.5×10^{39}	0.038	0.0058
Arp 256-1	1.69 ± 0.02	0.42 ± 0.01	2.42 ± 0.02	$6.3 \pm {}^{0.5}_{0.0}$	17.6×10^7	0.076	17.3×10^{39}	0.098	0.0065
Arp 270-1	0.97 ± 0.02	0.24 ± 0.01	1.39 ± 0.02	$5.9 \pm {}^{0.4}_{0.0}$	0.1×10^7	0.893	147.2×10^{39}	0.526	0.0795
Arp 270-2	1.63 ± 0.02	0.40 ± 0.01	2.33 ± 0.02	$6.2 \pm {}^{0.5}_{0.0}$	0.2×10^7	≤ 0.076	$\leq 15.9 \times 10^{39}$	...	≤ 0.0060
Arp 270-3	0.98 ± 0.02	0.24 ± 0.01	1.40 ± 0.02	$5.7 \pm {}^{0.1}_{0.0}$	0.2×10^7	≤ 0.031	$\leq 8.9 \times 10^{39}$	...	≤ 0.0045
Arp 270-4	0.73 ± 0.02	0.18 ± 0.01	1.04 ± 0.02	$5.3 \pm {}^{0.2}_{0.0}$	0.5×10^7	≤ 0.007	$\leq 2.1 \times 10^{39}$	...	≤ 0.0024
NGC 2207-1	4.12 ± 0.02	1.02 ± 0.01	5.90 ± 0.02	$5.7 \pm {}^{0.2}_{0.0}$	4.3×10^7	0.064	15.1×10^{39}	0.033	0.0074

[a] From $A_{H\alpha} = 2.5 \log[1 + 0.038 L_{24}/L_{H\alpha}]$ (Kennicutt et al. 2007).

[b] Using $A_V/E(B-V) = 4.05$ (Calzetti et al. 2000).

[c] Using $N_H(cm^{-2}) = 5.8 \times 10^{21} E(B-V)$ from Bohlin, Savage, & Drake (1978).

[d] From the Hα equivalent width, assuming an instantaneous burst.

[e] Obtained by scaling the observed i band flux (or HST F814W flux, if no SDSS i image available) to Starburst99 models assuming an instantaneous burst, using the age determined from the Hα equivalent width and the absorption determined from the Hα/24 μm flux ratio.

[f] The ratio of the 0.3 − 8 keV X-ray luminosity L_X to the Hα luminosity, corrected for extinction using the Hα/24 μm flux ratio as described in the text.

[g] The ratio of the extinction-corrected 0.3 − 8 keV luminosity to the SFR. When both estimates of SFR are available, the average value is used.

[h] Electron number density $n_e \times \sqrt{f}$, where f is the volume filling factor (see text for details). Note that these are not relevant if the X-ray source is a ULX, which is likely for Arp 270-1 and Arp 240-4 (see text).

[i] X-Ray Production Efficiency = L_X/L_{mech}.